

PAPER • OPEN ACCESS

## Zero-dimensional simulations of DC ns-pulsed plasma jet in N<sub>2</sub> at near atmospheric pressure: validation of the vibrational kinetics

To cite this article: Youfan He *et al* 2024 *Plasma Sources Sci. Technol.* **33** 115011

View the [article online](#) for updates and enhancements.

You may also like

- [Correlation between temperature distribution and changes in self-organized luminous pattern in an atmospheric pressure DC glow discharge with sheath gas flow](#)  
Toshiaki Miyazaki, Koichi Sasaki and Naoki Shirai
- [Plasma response to pulsed ion acoustic wave excitation](#)  
Chenyao Jin, Chi-Shung Yip, Wei Zhang et al.
- [Impact of overvoltage on the mode transition of the spark gap switch: from edge breakdown to stochastic breakdown](#)  
Weixi Luo, Chenhua Ren, Bangdou Huang et al.



**HIDEN ANALYTICAL**

# Analysis Solutions for your Plasma Research

**For Surface Science**

- ▶ Surface Analysis
- ▶ SIMS
- ▶ 3D depth Profiling
- ▶ Nanometre depth resolution

■ Compact SIMS

■ SIMS Workstation

■ Auto SIMS

**For Plasma Diagnostics**

- ▶ Plasma characterisation
- ▶ Customised systems to suit plasma Configuration
- ▶ Mass and energy analysis of plasma ions
- ▶ Characterisation of neutrals and radicals

■ ESPion

■ HPR-60 MBMS

■ EQP Series

Click to view our product catalogue

■ Knowledge ■ Experience ■ Expertise

Contact Hiden Analytical for further details:  
W [www.HidenAnalytical.com](http://www.HidenAnalytical.com)  
E [info@hiden.co.uk](mailto:info@hiden.co.uk)

# Zero-dimensional simulations of DC ns-pulsed plasma jet in N<sub>2</sub> at near atmospheric pressure: validation of the vibrational kinetics

Youfan He<sup>1,\*</sup> , Jan Kuhfeld<sup>2</sup> , Nikita D Lepikhin<sup>2</sup> , Uwe Czarnetzki<sup>2</sup> , Vasco Guerra<sup>3</sup> , Ralf Peter Brinkmann<sup>1</sup> , Andrew R Gibson<sup>4,5,\*</sup>  and Efe Kemaneci<sup>1,\*</sup> 

<sup>1</sup> Institute of Theoretical Electrical Engineering, Faculty of Electrical Engineering and Information Technology, Ruhr University Bochum, Bochum, Germany

<sup>2</sup> Experimental Physics V, Faculty of Physics and Astronomy, Ruhr University Bochum, Bochum, Germany

<sup>3</sup> Instituto de Plasmas e Fusão Nuclear, Instituto Superior Técnico, Universidade de Lisboa, Lisbon, Portugal

<sup>4</sup> Research Group for Biomedical Plasma Technology, Faculty of Electrical Engineering and Information Technology, Ruhr University Bochum, Bochum, Germany

<sup>5</sup> York Plasma Institute, School of Physics, Engineering and Technology, University of York, York, United Kingdom

E-mail: [heyoufan1993@gmail.com](mailto:heyoufan1993@gmail.com), [andrew.gibson@york.ac.uk](mailto:andrew.gibson@york.ac.uk) and [efekemaneci@gmail.com](mailto:efekemaneci@gmail.com)

Received 24 April 2024, revised 23 September 2024

Accepted for publication 23 October 2024

Published 15 November 2024



CrossMark

## Abstract

A Direct current (DC) nanosecond (ns)-pulsed plasma jet fed with N<sub>2</sub> at near atmospheric pressure (20 000 Pa) is studied using a transient zero-dimensional (0-D) model coupled with a two-term Boltzmann equation solver. Good agreement is observed between the simulated and measured plasma properties: including the electron density and the ratios of the N<sub>2</sub>( $v = 1, 2, 3, 4$ ) densities to the gas density. A variety of theoretical approaches are considered to determine the Vibrational-Vibrational (V-V) and Vibrational-Translational (V-T) rate coefficients. For the V-V kinetics, the simple form of an Harmonic Oscillator (sfHO), the Schwartz-Slawsky-Herzfeld (SSH) and the Forced Harmonic Oscillator (FHO) approaches are used. The SSH approach used in this study is an improved version based on the pure SSH approach. For the V-T kinetics, the sfHO, a fit function of the Semi-Classical (ffSC) calculations and a fit function of the Quasi-Classical Trajectory (ffQCT) calculations are used. The influence of these different approaches on the calculated temporal evolution profiles of the vibrational distribution functions (VDFs) within one pulse modulation cycle is revealed. It is observed that the use of these different approaches does not strongly affect the densities of the low vibrational levels ( $v < 5$ ), whereas larger influences on the higher level densities are found. In addition, it is found that the simulated evolution of the VDFs are sensitive to the probabilities of the neutral wall reaction  $N_2(v) + \text{wall} \rightarrow N_2(v-1)$  in the range of  $1 \times 10^{-2}$  to  $1 \times 10^{-4}$ . A further analysis of the wall quenching probabilities of  $N_2(0 < v < 58)$  is of importance for a more accurate prediction of the VDFs.

\* Authors to whom any correspondence should be addressed.



Original Content from this work may be used under the terms of the [Creative Commons Attribution 4.0 licence](https://creativecommons.org/licenses/by/4.0/). Any further distribution of this work must maintain attribution to the author(s) and the title of the work, journal citation and DOI.

Keywords: zero-dimensional model, DC ns-pulsed power, near atmospheric pressure plasma jet, nitrogen plasma validation, nitrogen V-V and V-T kinetics, nitrogen vibrational distribution function

## 1. Introduction

Atmospheric pressure plasmas have gained increasing attention in the last 20 years due to their efficient conversion of ordinary gases into diverse reactive species. The produced species are required by a broad range of applications: such as plasma medicine (e.g. wound healing [1], cancer therapy [2, 3] and skin wetting properties [4]), plasma-assisted catalysis (e.g. for CH<sub>4</sub> [5, 6], CO<sub>2</sub> [7, 8] conversion and for NH<sub>3</sub> synthesis [8–12]), material surface processes (e.g. glass cleaning [13, 14], polymer activation prior to adhesive bonding [15], tool steel hardening [16], TiO<sub>2</sub> films preparation for solar cells [17], water contact-angle reduction [18]). Various atmospheric pressure plasma sources were developed in parallel for use in these abundant application fields [19].

Atmospheric pressure plasma jets [20, 21] have the advantages of miniature and simple design. Additionally, reactive species are formed at close to ambient temperature due to the non-equilibrium between the highly energetic electrons and lower temperature heavy neutral particles. This enables these jet devices to treat heat-sensitive surfaces especially in the biomedical application field. It should be emphasized that a more uniform discharge structure is produced by the plasma jet relative to the other types of atmospheric pressure plasma sources [22], e.g. the corona and dielectric barrier discharge. A uniform structure of the electric field between the plane-to-plane electrodes in a direct current (DC) nanosecond (ns)-pulsed plasma jet has been shown by E-FISH measurements [23]. Good optical access for species density measurements is given by plasma jet chambers with simple geometries, such as rectangular structures with plane-to-plane electrodes [24–26]. These provide a suitable platform for a reliable validation between measurements and simulations of the plasma domain, e.g. the validations of helium metastable and reactive oxygen species [27], hydroxyl radical and atomic oxygen [28], ratios of the N<sub>2</sub>( $v = 1, 2, 3, 4$ ) densities to the gas density [29], atomic oxygen [30], helium metastable and atomic oxygen [31]. Diverse reactive species densities from various works in the literature are validated in our previous study [32]. A better understanding of the reactive species formation mechanisms is supported by the complementarity between the measurements and simulations. This contributes to a better control of the reactive species densities which is of importance for the application performance.

Pulse modulation has been widely used, e.g. it was applied in nitrogen plasma jets for diverse applications [33–37]. DC [29, 36–40] and alternating current [33–35, 41, 42] modulations were used during the power-on phase. Control of the reactive species density and the gas heating through the pulse modulation was presented by Kelly *et al* [41] and Dedrick *et al* [42]. It was predicted by Davies *et al* [38] that the nitrogen

vibrational state densities can be tailored by the pulse modulation. Large electron density values (e.g.  $\sim 10^{19} \text{ m}^{-3}$  [29, 39, 40]) are obtained by ns-pulsed power sources. The ignition of pure molecular gas at or near atmospheric pressure is facilitated by the instantaneously produced large amount of high energy electrons during the power-on phase. A stable glow discharge is maintained by the repetitive sequence of energy input from the pulses, and gas heating is simultaneously prevented as a result of the small time-averaged power value [25, 29]. It was experimentally shown in the nitrogen plasma jet [25, 29] that the abundant vibrational excitation is obtained in accordance with the large electron density values in the power-on phase, and the vibrationally excited nitrogen molecules survive for a long time in the power-off phase. These imply that an attractive path to efficiently produce vibrational states in a molecular gas is given by the power supply with a ns-pulsed modulation.

The vibrational distribution functions (VDFs) of molecular gases can play an important role in plasma applications. The N<sub>2</sub> dissociation, which represents a key challenge in NH<sub>3</sub> synthesis [12], is mainly manipulated by reaction channels containing N<sub>2</sub>( $v > 0$ ) [43]. It was also reported by Bogaerts and Erik [8] that the most energy-efficient N<sub>2</sub> dissociation pathway is provided by N<sub>2</sub>( $v > 0$ ). The significant role of N<sub>2</sub>( $v > 0$ ) in the N<sub>2</sub> dissociation is attributed to the reduced reaction energy barrier, in comparison with direct electron-impact dissociation of N<sub>2</sub>( $v = 0$ ). Moreover, NO is potentially important for biomedical applications, e.g. wound healing [1]. In our previous work [32], zero-dimensional (0-D) plasma-chemical kinetics simulations predicted that the N<sub>2</sub> VDF ( $v \geq 13$ ) has a more significant influence on the NO production at higher power values in the range of 0.5–2 W in the COST-Jet [44].

It is difficult to produce a stable glow discharge with pure molecular gases at atmospheric pressure. In order to yield the vibrational population of molecular gas in a stable discharge at atmospheric pressure, other works have used various approaches, e.g. a configuration of the pin-to-plane electrodes was used in the air plasma [45], or the molecular gas N<sub>2</sub> was mixed with noble gases [46, 47]. Therefore, detailed studies regarding N<sub>2</sub> VDFs have also been carried out in near atmospheric pressure discharges. For instance, validations between the measured and simulated N<sub>2</sub>( $v = 1, 2, 3, 4$ ) densities of ns-pulsed plasmas at pressures of  $1 \times 10^4 \text{ Pa}$ – $2 \times 10^4 \text{ Pa}$  were carried out by Vereshchagin *et al* [48], Montello *et al* [49], Shkurenkov *et al* [50], Yang *et al* [51] and Kuhfeld *et al* [25, 29]. The N<sub>2</sub>( $v = 1, 2, 3, 4$ ) density validation was conducted at three time points during the whole pulse modulation period [48], and the N<sub>2</sub>( $v = 1, 2, 3, 4$ ) concentrations were validated in filament pin-to-pin discharges [49–51]. Recently, a relatively homogeneous discharge in a DC ns-pulsed N<sub>2</sub> plasma jet

with plane-to-plane electrodes was reported [25] and further confirmed [52, 53]. The  $N_2(v=1,2,3,4)$  densities in the power-off phase were validated [25, 29]. However, a more comprehensive validation between the measured and simulated  $N_2$  VDFs considering, for example, the entire pulse cycle and simultaneous cross-validation with the electron density for various operating conditions, is still missing. Therefore, the measured  $N_2(v=1,2,3,4)$  densities during the whole pulse cycle and the corresponding electron density with a variation of the power-on duration and peak power value in [25, 29] are extremely suitable for a further validation of the model calculations.

The shape of the VDFs in  $N_2$  is determined by the state-to-state vibrational kinetics. Due to a treatment of each vibrational level as a separate species, the rate coefficients of respective vibrational level reacting with other species are properly considered in the simulation to further output a reasonable shape of the VDFs. In order to provide a complete picture of the VDFs, dozens of vibrational levels and the resulting thousands of reactions in the detailed vibrational kinetics are included in the chemical model. The 0-D model as introduced in [32] is a proper tool for an efficient analysis of the aforementioned complex chemical aspects. Furthermore, diverse theoretical approaches to calculate the individual rate coefficients involved in the state-to-state vibrational kinetics have been reported in the literature, see details in section 4. A challenge still to be addressed is a clarification of the influence of these diverse approaches on the plasma properties and the calculated  $N_2$  VDFs.

The main aims of this work are divided into the following two phases:

- A reliable validation of the electron density and the corresponding ratios of the  $N_2(v=1,2,3,4)$  densities to the gas density is obtained in section 5.1, by taking advantage of the relatively uniform discharge produced by a plasma jet with plane-to-plane electrodes. This validation is thoroughly conducted in the whole modulation period of the DC ns-pulsed plasma jet fed with pure nitrogen gas at near atmospheric pressure, and also conducted with a variation of the power-on duration and peak power value.
- The role of diverse theoretical approaches for the calculation of the rate coefficients related to the state-to-state vibrational kinetics in determining the temporal evolution of the electron density and the  $N_2$  VDFs is revealed in sections 5.1–5.4.

The details of the plasma jet simulated in this work are described in section 2. The developed transient 0-D model is explained in section 3, and the considered chemical kinetics are reported in section 4. The sensitivity of the  $N_2$  VDF evolution profiles to varying numbers of vibrational levels incorporated in the chemical model and to the neutral wall reaction probabilities is addressed in sections 5.5 and 5.6, respectively. The key results are concluded in section 6.

## 2. Experimental model system

A DC ns-pulsed plasma jet fed with  $N_2$  at near atmospheric pressure is simulated in this study, and illustrated in figure 1. The jet is described in detail in [25, 29]. The  $1 \times 1 \times 20 \text{ mm}^3$  rectangular plasma chamber is constructed with two planar electrodes and two side glass plates. The feed gas is injected through one orifice located in the middle of one glass plate, and the effluent is exhausted from the two non-surrounded and smallest cross sections (i.e.  $1 \times 1 \text{ mm}^2$ ). The setup is designed as a cross-field configuration, i.e. the generated electric field is perpendicular to the feed gas flow. The simulation results in this work are compared with the electron density (calculated from the measured current and electric field) and the measured ratios of the  $N_2(v=1,2,3,4)$  densities to the gas density reported in [25, 29]. The feed gas flow rate was set as 20 sccm  $N_2$  at a pressure of 20 000 Pa. The plasma was driven by a 1 kHz pulsed DC waveform with a variable power-on duration & peak power value. The parameters used in this study were (a) 200 ns & 17 kW see figure 4, (b) 250 ns & 17 kW and (c) 200 ns & 29 kW see figures B1 and B2 in appendix B, respectively. For the sake of simplicity, the power set (a) 200 ns and 17 kW is considered in all the simulation results in section 5, whereas the sets (b) and (c) are merely used in appendix B. It was reported in [25] (P. 11) that the rotational temperature is around 330 K in the case of these three power sets, and is expected to stay constant during the whole pulse cycle. The gas temperature is assumed to be equal to the rotational temperature [25] (P. 4). Therefore,  $T_g = 330 \text{ K}$  is used in all the simulations of this study. For the conditions studied in this work (parameters used to calculate Knudsen number), the Knudsen number is approximately  $0.4556 \times 10^{-3}$ , which implies no-slip velocity and no-temperature jump at the walls of the jet [54] (P. 3453).

The absorbed power density is one essential input parameter defining the plasma properties. It is of importance for a reliable validation that the absorbed power density in the 0-D simulations is a good representation of that in the measurements. The DC ns-pulsed absorbed power profiles used in this work (i.e. the power dissipated in the whole plasma volume) are obtained from a multiplication between the voltage and current measured in [25]. As a result of the DC power, the voltage drop was mainly applied to one of the two planar electrodes in the near atmospheric pressure  $N_2$  plasma jet [25, 29]. Consequently, much more energetic electrons are accumulated near the powered electrode relative to the grounded electrode [52] (P. 7). It was also shown in [52] (P. 7) that the plasma volume is likely divided into two regions: (i) a region with a spatially non-uniform electron density distribution on the side of the powered electrode, and (ii) a region with a spatially quasi-uniform electron density distribution on the side of the grounded electrode. The latter was also hinted in [25] (P. 9) that around 80% of the plasma volume of the nitrogen discharge is captured as a homogeneous structure by an ICCD image. Furthermore, such a percentage value for the ratio of the homogeneous region to the total plasma volume is also recently confirmed in [52, 53].

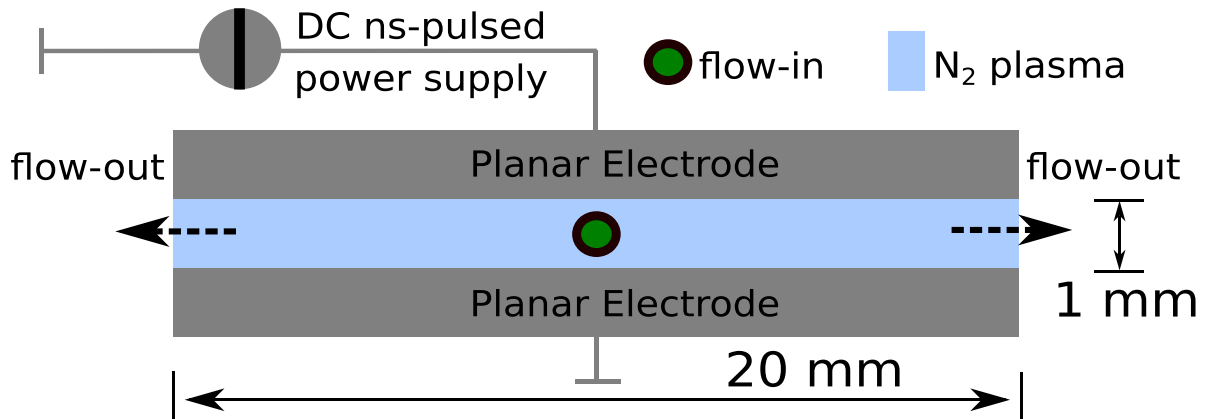


**Figure 1.** Schematic structure of the DC ns-pulsed plasma jet simulated in this work. The  $1 \times 1 \times 20 \text{ mm}^3$  rectangular capillary plasma chamber consists of two planar electrodes and two side glass plates. The chamber is fed with  $\text{N}_2$  gas through one orifice located in the middle of one glass plate [25, 29]. The details of the operating conditions are given in section 2. The figure is not drawn to scale.

It should be emphasized that both the constant electric field (used to calculate the electron density [29]) and the ratios of the  $\text{N}_2(v=1, 2, 3, 4)$  densities to the gas density [25] were measured in the aforementioned homogeneous region between two electrodes and averaged along the gas flow direction. In other words, both the electron density and the density ratios from the measurement data of the  $\text{N}_2$  plasma are considered to be the volume-averaged values in this homogeneous region. Furthermore, it was indicated in [25] that around 35% of the total absorbed power is distributed to this homogeneous region. Therefore, the absorbed power density (see equation (8)) in this homogeneous region is used as an input to the 0-D simulations of the plasma source in section 5 and appendix B, i.e.:

$$Q_{\text{abs}, \text{N}_2} = (35\%P_{\text{abs}}) / (80\%V) = 43.75\%P_{\text{abs}}/V, \quad (1)$$

where  $P_{\text{abs}}$  is the absorbed power in the whole plasma volume  $V$ . Our simulation results are compared well with the aforementioned measured electron density and vibrational level density ratios [25, 29], see figures 4, B1 and B2. It is worth to note that similar electron density values were also reported in [52, 53]. The other 65% of the total absorbed power distributed into the other 20% volume of the  $\text{N}_2$  discharge is likely more favorable for electronic excitation and ionization than for vibrational excitation due to the present high electric field in the sheath on the side of the powered electrode and the resulting highly energetic electrons [25]. In other words, the nitrogen vibrational level densities in the aforementioned homogeneous region are likely not affected by the other 65% of the total absorbed power.

### 3. Model

The particle balance equations and an electron energy balance equation are solved in a volume-averaged 0-D model formalism [55–57] to compute the time-resolved charged and neutral species densities and effective electron temperature (see considered species in table 1). Only a brief summary of

the model is provided here and further details can be found in an earlier study [32]. The model is coupled with a two-term Boltzmann solver, *LisbOn Kinetics Boltzmann* (LoKI-B) [58], to self-consistently calculate the electron energy distribution function (EEDF). The time to reach a steady-state distribution function at atmospheric pressure is in the order of a few nanoseconds, which is confirmed by kinetic models [59, 60]. Therefore, the consecutive stationary solutions of the Boltzmann equation are used in the simulations of each pulse, which is similarly implemented in various transient models of the nanosecond range time-scales [61–63]. Specifically, the time-variation of the plasma composition calculated in the 0-D simulations is fed-into the computations of the Boltzmann solver for a self-consistent evolution of the electron kinetics during the pulse. These computations are updated as the power varies at 0 ns, 65 ns, 100 ns and 300 ns in figures 4 and B2 (at 0 ns, 65 ns, 100 ns and 350 ns in figure B1). At 0 ns is the start of each pulse, around 65 ns is the peak power value, about 100 ns is the start of the plateau-power phase, roughly 300 ns and 350 ns are the end of the power-on phase (see details in section 5.1). These time points are chosen due to a drastic change of the power value relative to each other. Note that tests have been carried out with more frequent updates of the Boltzmann solver, i.e. the updates are carried out for every 5–10 ns during the power-on phase. The simulation results with these more frequent updates do not significantly change relative to those with updates only at above-mentioned four time points, e.g. such a change for the electron density in the power-on phase of figure 4 is below 2%. After each update of the Boltzmann solver, the look-up tables of the considered electron-impact reactions are accordingly updated. Each table consists of the effective electron temperatures and the corresponding rate coefficients. These effective electron temperatures are derived from the mean electron energy of the non-Maxwellian EEDFs. These EEDFs are calculated by the Boltzmann solver for a range of values of the applied reduced electric field, i.e. each reduced electric field value corresponds to a consequent non-Maxwellian EEDF and its effective electron temperature (The current formulation follows the local

mean energy approximation [64] (P. 3) and [65] (P. 3906)). In accordance with the updated look-up tables at the above-mentioned four time points, the particle and electron energy balance equations are solved to compute the plasma properties such as the time-resolved electron density and effective electron temperature. Super-elastic collisions are incorporated in the electron kinetics to better resolve the EEDF [66], and considered in the particle balance equations and the electron energy balance equation.

In consideration of the residence time of the feed gas in the jet chamber (i.e. the chamber length divided by the gas flow velocity, see equation (5) in [32]), only 6 pulses are simulated for the plasma jet considered in this work. Thus, the simulations start with an initial gas density: i.e. the feed gas density at the entrance of the plasma chamber. Specifically, the  $N_2(v=0)$  density is calculated by the ideal gas law, and the densities of the other species considered in this work are numerically set to 0. The simulations are carried out at a constant gas temperature  $T_g$ , which was experimentally defined [25].

The volume-averaged particle balance equation of a species  $i$  is given by

$$\frac{dn_i}{dt} = \sum_j \mathcal{W}_{ij} R_i^j \Big|_V + \sum_j \mathcal{W}_{ij} R_i^j \Big|_W, \quad (2)$$

where  $n_i$  is the density,  $j$  a reaction,  $R_i^j$  the reaction rate and  $\mathcal{W}_{ij}$  the net stoichiometric coefficient. The chemical reactions are divided into two parts: subscript ‘ $v$ ’ denotes those inside the plasma volume and ‘ $w$ ’ those at the wall surface.

The volume reaction rate of species  $i$  in a reaction  $j$  is

$$R_i^j \Big|_V = k^j \prod_l n_l^{\nu_{lj}}, \quad (3)$$

where  $l$  denotes all the reactants,  $\nu_{lj}$  the forward stoichiometric coefficient and  $k^j$  the rate coefficient. The flow-in rate of the feed  $N_2$  gas and the flow-out rates of species  $i$  are [32]

$$R_i^{\text{F-in}} \Big|_W = c \frac{QP_{\text{atm}}}{V k_B T_{\text{in}}}, \quad (4)$$

$$R_i^{\text{F-out}} \Big|_W = cQ \frac{P_{\text{atm}} T_g}{V P T_{\text{in}}} n_i, \quad (5)$$

where  $Q$  (sccm) is the net mass flow rate,  $c$  the unit conversion factor,  $P_{\text{atm}}$  the atmospheric pressure,  $V$  the plasma volume,  $T_{\text{in}}$  the feed gas temperature,  $T_g$  the gas temperature of plasma and  $P$  the pressure in the plasma chamber.

The ion mobility is limited in the case of highly collisional plasmas, and the ion speed at the sheath edge is smaller than the Bohm velocity [67] (P. 173). At (or near) atmospheric pressure, the ion speed is particularly small due to the extremely small mean free path. Furthermore, the ion wall reaction rates (see equation (6) in [32]) are proved to play a negligible role in the simulation results of our previous work [32] and of this work. Therefore, the wall loss of ions is not considered in this study. The wall loss of a neutral species  $i$  is defined as [32, 68]

$$R_i^N \Big|_W = n_i \left( \frac{\Lambda_0^2}{D_i} + \frac{2V(2-\gamma_i)}{2(A_X+A_Y)v_i\gamma_i} \right)^{-1}, \quad (6)$$

where  $X$  and  $Y$  are the plasma dimensions,  $A_X$  and  $A_Y$  the wall surface areas,  $\gamma_i$  the wall reaction probability,  $v_i$  the mean neutral velocity,  $\Lambda_0$  the effective diffusion length in Cartesian coordinates,  $D_i$  the diffusion coefficient [67] (P. 134) as a function of the mean free path [69] (P. 3) calculated by the  $N_2$ - $N_2$  collision cross-section [70] (P. 6). The dissociation degree of nitrogen molecules under the operating conditions investigated in this study is below 0.1%. In other words, the simulated nitrogen atom density is at least three orders of magnitude smaller than the simulated nitrogen molecule density over the whole pulse period. Based on the cross-section value of the dominant  $N_2$ - $N_2$  collision, the same mean free path is assigned to each neutral species (including nitrogen atoms) considered in the wall losses. Note that the diffusion coefficients as a function of the neutral species mass distinguish from each other.

The volume-averaged electron energy balance equation for an electron density  $n_e$  and effective electron temperature  $T_e$  is [32]

$$\frac{d}{dt} \left( \frac{3}{2} n_e T_e \right) = Q_{\text{abs}} - (Q_{\text{Che}} + Q_{\text{Ela}}), \quad (7)$$

where  $Q_{\text{abs}}$  is the absorbed power density,  $Q_{\text{Che}}$  is the energy loss in chemical reactions and  $Q_{\text{Ela}}$  is the energy loss in elastic collisions. The absorbed power density is

$$Q_{\text{abs}} = P_{\text{abs}}/V, \quad (8)$$

where  $P_{\text{abs}}$  is the absorbed power in the whole plasma volume  $V$ . Note that only part of  $P_{\text{abs}}$  and part of  $V$  are considered to calculate the absorbed power density of the homogeneous discharge region simulated in this study, see equation (1). The electron energy loss from the chemical processes is

$$Q_{\text{Che}} = \sum_j \mathcal{E}_j R_e^j \Big|_V, \quad (9)$$

where the summation is over electronic process  $j$  with the energy  $\mathcal{E}_j$  and the rate  $R_e^j$ . The electron energy loss in the elastic collisions is [69, 71]

$$Q_{\text{Ela}} = \sum_i n_e n_i 3T_e \frac{m_e}{m_i} k_{ei}^{\text{El}}, \quad (10)$$

where  $m$  is the mass of a particle, and  $k_{ei}^{\text{El}}$  represents the elastic rate coefficients in the look-up tables updated by LoKI-B. For further details, see [32].

#### 4. Chemical kinetics

The set of species considered in the  $N_2$  plasma are given in table 1. All the chemical kinetics included in this work together with the updates and supplements compared to those in our previous work [32] are provided in appendix A. The

**Table 1.** The species involved in the N<sub>2</sub> chemical model. Each vibrational level N<sub>2</sub>(0 < v < 58) is treated as a separate species. A pseudo level N<sub>2</sub>(v' = 58) is considered to instantaneously dissociate to two nitrogen atoms due to the proximity of its vibrational energy to the dissociation energy [32], see table A5.

N <sub>2</sub> plasma: N <sub>2</sub> (v = 0), N <sub>2</sub> (A <sup>3</sup> Σ), N <sub>2</sub> (B <sup>3</sup> Π), N( <sup>4</sup> S), N( <sup>2</sup> D), N <sup>+</sup> , N <sub>2</sub> <sup>+</sup> , N <sub>3</sub> <sup>+</sup> , N <sub>4</sub> <sup>+</sup> , N <sub>2</sub> (0 < v < 58), e
-----
Additionally considered species in this work compared to [32]: N <sub>2</sub> (W <sup>3</sup> Δ), N <sub>2</sub> (B' <sup>3</sup> Σ), N <sub>2</sub> (a' <sup>1</sup> Σ), N <sub>2</sub> (a <sup>1</sup> Π), N <sub>2</sub> (w <sup>1</sup> Δ), N <sub>2</sub> (C <sup>3</sup> Π), N <sub>2</sub> (E <sup>3</sup> Σ), N <sub>2</sub> (a'' <sup>1</sup> Σ), N <sub>2</sub> (singlets*), N( <sup>2</sup> P), N <sub>2</sub> <sup>+</sup> (B)

chemical set including the reactions and their rate coefficients are similar to those published in a previous study [32], where simulations of radio-frequency plasmas are validated against a large variety of measurement data. The exception is that some rate coefficients for volume reactions and nitrogen vibrational kinetics are updated as remarked in tables A1 and A2 of appendix A, respectively. Specifically, those of reactions 17, 18 and 48 in table A1 are updated as these were found to better describe the electron density decay rate during the power decay of the power-on phase depicted in figure 4(a) and the ratio of N<sub>4</sub><sup>+</sup> density to N<sub>2</sub><sup>+</sup> density (not shown here). Furthermore, besides N<sub>2</sub>(A<sup>3</sup>Σ<sub>u</sub><sup>+</sup>), N<sub>2</sub>(B<sup>3</sup>Π<sub>g</sub>) and N(<sup>2</sup>D) in [32], the higher electronically excited states (including N<sub>2</sub>(W<sup>3</sup>Δ<sub>u</sub>), N<sub>2</sub>(B'<sup>3</sup>Σ<sub>u</sub><sup>-</sup>), N<sub>2</sub>(a'<sup>1</sup>Σ<sub>u</sub><sup>-</sup>), N<sub>2</sub>(a<sup>1</sup>Π<sub>g</sub>), N<sub>2</sub>(w<sup>1</sup>Δ<sub>u</sub>), N<sub>2</sub>(C<sup>3</sup>Π<sub>u</sub>), N<sub>2</sub>(E<sup>3</sup>Σ<sub>g</sub><sup>+</sup>), N<sub>2</sub>(a''<sup>1</sup>Σ<sub>g</sub><sup>+</sup>), N<sub>2</sub>(higher – singlets) and N(<sup>2</sup>P)) are additionally considered in this work (see also notes in tables A3 and A4 as well as discussion in appendix C). The electron-impact reactions (related to these states and the nitrogen ion N<sub>2</sub><sup>+</sup>(B)) are considered in the 0-D model and LoKI-B solver in accordance with the complete set of the IST-Lisbon database, which yields calculated swarm parameters in good agreement with measurements for E/N values between 1 and 1000 Td [72]. A better quantitative agreement between the measured and simulated electron density in figure 4(a) is obtained through such considerations. The neutral-neutral reactions related to these additionally considered species are mainly adopted from the work of Levaton *et al* [73]. A list of these additionally considered electron-impact and neutral-neutral reactions is shown in table A3. The neutral wall reactions in this work are provided in table A4. The wall reaction probability  $\gamma = 1$  of N<sub>2</sub>(v) + wall → N<sub>2</sub>(v - 1) used in [32] (referring to a simulation study [70]) is updated in this work with  $\gamma = 3 \times 10^{-3}$  (based on an experimental work [74] which gives a range of  $4 \times 10^{-4}$  to  $3 \times 10^{-3}$  for the wall deactivation probabilities of N<sub>2</sub>(v = 1) under different surface materials and operating conditions).  $\gamma = 3 \times 10^{-3}$ , as the maximal value, is chosen for the wall deactivation probabilities of N<sub>2</sub>(0 < v < 58) in the simulations of section 5 and appendix B, if not stated otherwise (see table 3). The N<sub>2</sub> reactions, which are consistent with those in [32], are given in tables A5 and A6 considering the pseudo level N<sub>2</sub>(v' = 58) dissociation and the elastic collisions, respectively.

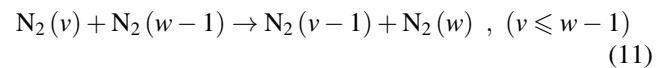
In the current study, the simulation results of a ns-pulsed nitrogen plasma are validated against the time-resolved measurement data of the electron density and the ratios of the

N<sub>2</sub>(v = 1, 2, 3, 4) densities to the gas density recently reported by Kuhfeld *et al* [25, 29]. It should be emphasized that the accurate measurements of higher vibrational levels are not available as a result of weaker signal [25]. Hence, a validation of the whole N<sub>2</sub>(0 < v < 58) VDF is not accessible.

An investigation of the established vibrational kinetics is the focus of this work. The vibrational kinetics included in the model consist of the electron-Vibrational (e-V), Vibrational-Vibrational (V-V) and Vibrational-Translational (V-T) mechanisms. The e-V kinetics (identical to those of [32]) adopt the resonant vibrational excitation cross-sections of Laporta *et al* [75] as well as the dissociation and ionization processes in the Phys4Entry database [76]. Several distinct methods exist in the literature to approximate the V-V and V-T rate coefficients, and their details are discussed below in sections 4.1–4.4. The role of these approximations in the ns-pulsed plasma jet calculations is presented in sections 5.1–5.4 and appendix B.

#### 4.1. V-V kinetics

The rate coefficients  $k_{v,v-1}^{w-1,w}$  of the N<sub>2</sub>-N<sub>2</sub> V-V reactions



are calculated by multiplying  $k_{1,0}^{0,1}$  by a scaling factor  $s_{v,v-1}^{w-1,w}$ . Three conventional scaling laws are used to calculate  $s_{v,v-1}^{w-1,w}$ :

- (1) The simple form for an Harmonic Oscillator (sfHO) was provided and the corresponding scaling factor was given as [77] (P. 11)

$$s_{v,v-1}^{w-1,w} = vw. \quad (12)$$

- (2) The Schwartz-Slawsky-Herzfeld (SSH) model [78] was modified by Bray [79] and the analytical expression was further summarized by Alves *et al* [80] (P. 9). The basic form of the scaling factor was reported as

$$[s]_{v,v-1}^{w-1,w} = vw \left( \frac{1 - \chi_{e,N_2}}{1 - \chi_{e,N_2}v} \right) \left( \frac{1 - \chi_{e,N_2}}{1 - \chi_{e,N_2}w} \right) \frac{F(Y_{v,v-1}^{w-1,w})}{F(Y_{1,0}^{0,1})}, \quad (13)$$

where  $\chi_{e,N_2} = \frac{\omega_{e,N_2} \chi_{e,N_2}}{\omega_{e,N_2}} = \frac{14.324 \text{ cm}^{-1}}{2358.57 \text{ cm}^{-1}} = 6.073 \times 10^{-3}$  is the first anharmonicity constant of the oscillator nitrogen

molecule in electronic ground state [81] (P. 687), and  $F(Y)$  is the adiabaticity factor evaluated as [82] (P. 2291)

$$F(y) \simeq \begin{cases} \frac{1}{2} [3 - e^{-2y/3}] e^{-2y/3}, & y \leq 20 \\ 8 \left(\frac{\pi}{3}\right)^{1/2} y^{7/3} e^{-3y^{2/3}}, & y > 20 \end{cases} \quad (14)$$

The intermediate parameter  $Y_{v,v-1}^{w-1,w}$  is defined as

$$Y_{v,v-1}^{w-1,w} = \left| \Delta E_{v,v-1}^{w-1,w} \right| \frac{\pi L}{\hbar} \sqrt{\frac{\mu}{2k_B T_g}}, \quad (15)$$

where  $\left| \Delta E_{v,v-1}^{w-1,w} \right| = |E_{v-1} + E_w - E_v - E_{w-1}|$  is the released energy of the exothermic V-V reactions (11),  $E_v$  is the internal energy of the nitrogen vibrational level  $v$  [75],  $L = 2 \times 10^{-11}$  m is the characteristic length for the short-range repulsive potential [83] (P. 109 115),  $\hbar$  the reduced Planck's constant,  $\mu$  the reduced mass of two-body collision,  $k_B$  the Boltzmann constant and  $T_g$  the gas temperature.

In this work, for cases where  $v \leq w - 1$ , i.e. exothermic reactions, the basic scaling factor  $[s]_{v,v-1}^{w-1,w}$  is multiplied by an exponential factor, as described by Loureiro and Ferreira [84] (P. 22), to give the final scaling factor

$$s_{v,v-1}^{w-1,w} = [s]_{v,v-1}^{w-1,w} \exp\left(\frac{-\Delta E_{v,v-1}^{w-1,w}}{k_B T_g}\right). \quad (16)$$

Note that  $\Delta E_{v,v-1}^{w-1,w} = E_{v-1} + E_w - E_v - E_{w-1} < 0$ , and the final scaling factor  $s_{v,v-1}^{w-1,w}$  is the pure SSH approach.

- (3) The Forced Harmonic Oscillator (FHO) model was discussed by Adamovich *et al* [85, 86] and later analytically given by Ahn *et al* [87]. Through the calculation of  $k_{v,v-1}^{w-1,w}/k_{1,0}^{0,1}$ , the obtained scaling factor (recently also adopted by Kuhfeld *et al* [29]) is

$$s_{v,v-1}^{w-1,w} = v w \frac{3 - e^{-\frac{2\lambda}{3}}}{2} e^{-\frac{2\lambda}{3}} \exp\left(\frac{-\Delta E_{v,v-1}^{w-1,w}}{2k_B T_g}\right) \quad (17)$$

with

$$\lambda = \frac{1}{3\sqrt{2}} \sqrt{\frac{\theta}{T_g}} \frac{|\Delta E_{v,v-1}^{w-1,w}|}{\omega_{e,N_2} \hbar}, \quad (18)$$

where  $\theta = (4\pi^2 \omega_{e,N_2}^2 \mu) / (\alpha^2 k_B)$ ,  $\omega_{e,N_2} = (2359 \text{ cm}^{-1}) \times (3 \times 10^{10} \text{ cm s}^{-1}) = 7.077 \times 10^{13} \text{ s}^{-1}$  is the oscillator frequency [88],  $\alpha = 4 \times 10^{10} \text{ m}^{-1}$  is the potential parameter between the interaction of two nitrogen molecules [89] (P. 396).

$k_{1,0}^{0,1} = 6.35 \times 10^{-23} T_g^{1.5} \text{ m}^3 \text{ s}^{-1}$  is used in case of implementing the sfHO and the SSH scaling laws in the simulations (following the value in [77, 80]). The obtained sfHO and SSH rate coefficients  $k_{v,v-1}^{w-1,w} = k_{1,0}^{0,1} s_{v,v-1}^{w-1,w}$  are further divided by a normalization factor

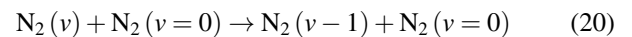
$$\xi_{vV} = \begin{cases} 39.0625 - 1.5625 \max(v, w), & \text{if } \max(v, w) < 10 \\ 25.2 + 24.1 \left(\frac{\max(v, w) - 10}{30}\right)^3, & \text{otherwise} \end{cases} \quad (19)$$

The factor  $\xi_{vV}$  is introduced so that the calculated rate coefficient values for the sfHO and the SSH scaling laws are improved, and these values of the improved version conform better with the semi-classical calculations reported by Billing and Fisher [89] (see figures 2(a)–(c)). Note that  $\xi_{vV}$  as a function of  $v$  and  $w$  typically reduces  $k_{v,v-1}^{w-1,w}$  by a factor of around 25–124, and this results in a reduced up-pumping effect of the V-V kinetics.  $k_{1,0}^{0,1} = 0.9 \times 10^{-20} \text{ m}^3 \text{ s}^{-1}$  is adopted in case of the FHO implementation (following the value in [29, 87]). It should be emphasized that  $k_{1,0}^{0,1} = 0.9 \times 10^{-20} \text{ m}^3 \text{ s}^{-1}$  chosen from a look-up table in [89] is solely valid at  $T_g = 300$  K. However, it is the closest value to the measured gas temperature  $T_g = 330$  K [25], which is adopted in the nitrogen plasma simulations in section 5 and appendix B.

The influences of the above-mentioned three different scaling laws (i.e. the sfHO, the SSH and the FHO) on the V-V rate coefficients  $k_{1,0}^{v-1,v}$ ,  $k_{6,5}^{v-1,v}$ ,  $k_{11,10}^{v-1,v}$  and  $k_{v,v-1}^{v,v+1}$  are presented in figures 2(a)–(d), respectively. These rate coefficients are additionally compared with the comprehensive and reliable data of the semi-classical calculations available from Billing and Fisher [89] and Capitelli [90] (P. 105), [91]. In the case of  $k_{1,0}^{v-1,v}$ ,  $k_{6,5}^{v-1,v}$  and  $k_{11,10}^{v-1,v}$ , the sfHO rate coefficients are larger than the SSH and the FHO ones as well as the semi-classical calculations [89, 90] (P. 105), [91] especially at higher vibrational levels. A relatively good agreement is acquired between the SSH and the FHO calculations. Both agree well with the available semi-classical calculations [89, 90] (P. 105), [91] in the range of  $v \leq 40$ . However, the sfHO rate coefficients are similar to the SSH and the FHO ones as well as the semi-classical calculations [90] (P. 105), [91] in the case of  $k_{v,v-1}^{v,v+1}$  in figure 2(d), i.e. the respective vibrational quantum number of both reactants is close to each other. This is also indicated by the rate coefficient values at low vibrational levels in figures 2(a)–(c). The influences of the sfHO, the SSH and the FHO V-V rate coefficients on the validated electron density and  $N_2(v = 1, 2, 3, 4)$  densities as well as on the calculated whole  $N_2$  VDF evolution profiles are revealed in sections 5.1 and 5.2.

#### 4.2. V-T kinetics

The rate coefficients  $k_{v,v-1}$  of the  $N_2$ - $N_2$  V-T reactions



are computed with  $k_{v,v-1} = k_{1,0} s_{v,v-1}$ , where  $s_{v,v-1}$  is the scaling factor provided as follows:

- (1) The sfHO scaling law was given as [77] (P. 11)

$$s_{v,v-1} = v. \quad (21)$$

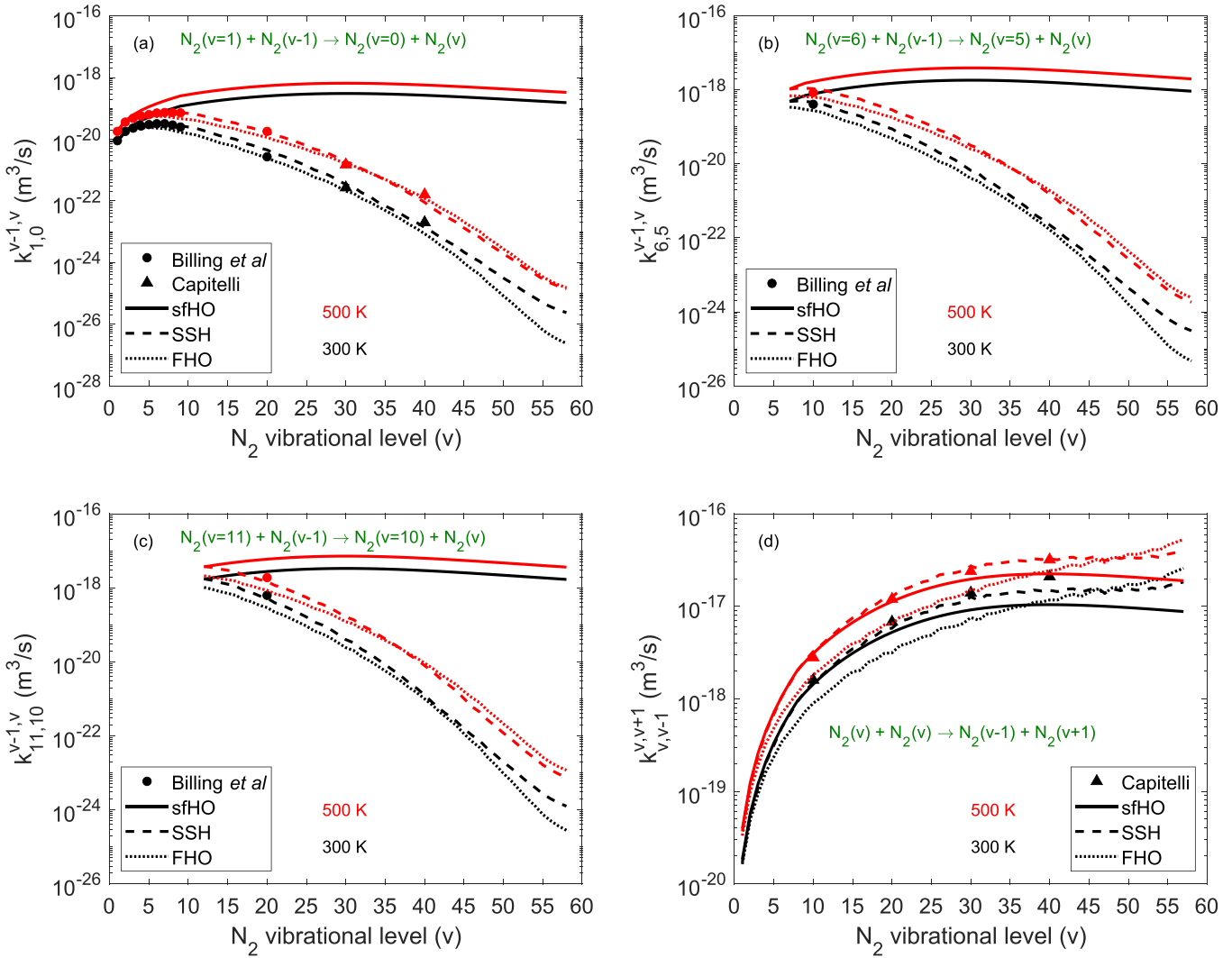


**Figure 2.**  $N_2$ - $N_2$  V-V rate coefficients (a)  $k_{1,0}^{v-1,v}$ , (b)  $k_{6,5}^{v-1,v}$ , (c)  $k_{11,10}^{v-1,v}$  and (d)  $k_{v,v-1}^{v,v+1}$  calculated with the sfHO (—), the SSH (---) and the FHO (.....) scaling laws (see section 4.1). The values from the available semi-classical calculations of Billing and Fisher [89] (●) and Capitelli [90] (P. 105), [91] (▲) are shown for comparison. The rate coefficients at  $T_g = 300$  K (black lines) and 500 K (red lines) are provided for a typical gas temperature range for plasma jets.

- (2) A scaling law, a fit function to the Semi-Classical (ffSC) calculations of Billing and Fisher [89], was recently reported by Richards *et al* [47] (P. 14):

$$s_{v,v-1} = v \exp\left((v-1)1.94/T_g^{\frac{1}{3}}\right). \quad (22)$$

Note that an agreement with the  $N_2$ - $N_2$  V-T rate coefficients from the semi-classical calculations of Billing and Fisher [89] is pursued both by those calculated from the SSH [77, 80] and the FHO [85, 86] approaches. Such an agreement is also observed for the  $N_2$ - $N_2$  V-V rate coefficients calculated with the SSH and the FHO approaches, see section 4.1. However, the considered V-V rate coefficients in this work can be only partially shown in figure 2 ascribed to their complexity, whereas the considered V-T rate coefficients can be fully presented in figure 3(a) attributed to their simplicity. Therefore, a potential difference between the simulation results using the SSH and the

FHO V-V kinetics is worthy of further investigation, while that using the SSH and the FHO V-T kinetics is not. In other words, a comparison between the SSH and the FHO approaches is much less valuable for the simple V-T collisions (relative to for the complex V-V collisions). For the sake of simplicity in this work, a comparison among the sfHO, the SSH and the FHO  $N_2$ - $N_2$  V-V kinetics is investigated, whereas for the  $N_2$ - $N_2$  V-T kinetics the simple approach sfHO is only compared to the ffSC approach directly tracing the semi-classical calculations in [89]. It is worth to note that the semi-classical calculations of the  $N_2$ - $N_2$  V-T rate coefficients for  $v \leq 20$  were calculated in [89]. Additional semi-classical calculations for  $v = 30, 40$  were provided by Capitelli [90] (P. 104), [91].

In case of the sfHO implementation, the  $k_{1,0}$  value is adopted from the work of Capitelli *et al* [83] (see table 7.1 on P.107) following the previous study [32]:

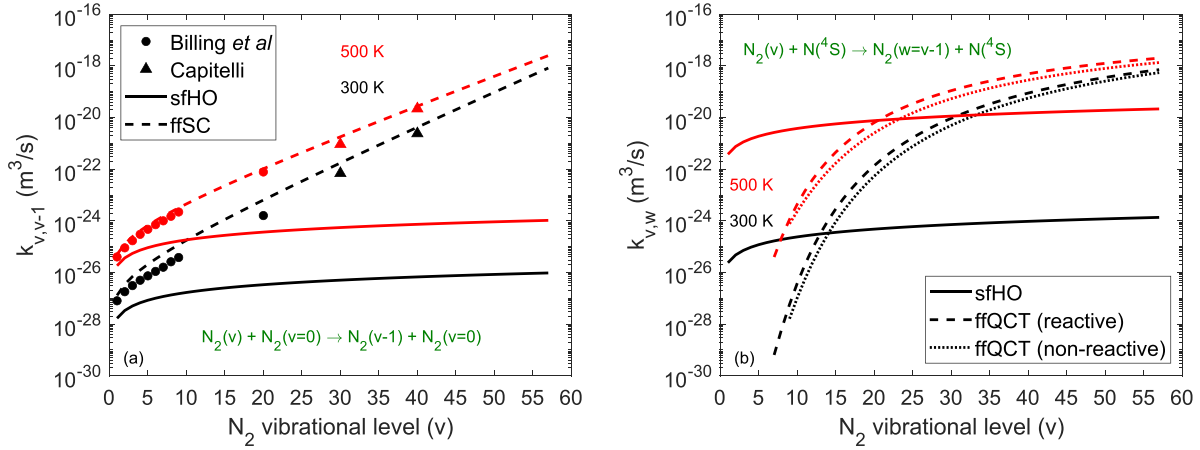


**Figure 3.** (a)  $\text{N}_2$ - $\text{N}_2$  V-T rate coefficients  $k_{v,v-1}$  calculated with the sfHO (—) and the ffSC (---), and the values from the available semi-classical calculations of Billing and Fisher [89] (●) and Capitelli [90] (P. 104), [91] (▲) for the purpose of comparison. (b)  $\text{N}_2$ - $\text{N}(^4\text{S})$  V-T rate coefficients  $k_{v,w}$  at  $v - w = 1$  calculated with the sfHO (—) and the ffQCT (---, ·····) for the reactive and non-reactive collision, respectively). For further details, see section 4.2. The rate coefficients at  $T_g = 300$  K (black lines) and 500 K (red lines) are provided for a typical gas temperature range for plasma jets.

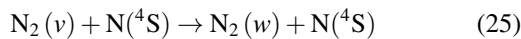
$$k_{1,0} = 7.8 \times 10^{-18} T_g \exp\left(-218/T_g^{1/3} + 690/T_g\right) \times [1 - \exp(-3340.8/T_g)]^{-1} \text{ m}^3 \text{ s}^{-1}, \quad (23)$$

whereas the  $k_{1,0}$  value in case of implementing the ffSC approach [47] (P. 14) is:

$$k_{1,0} = 3 \times 10^{-10} \exp\left(-400/T_g^{1/3} + 886/T_g^{2/3}\right) \text{ m}^3 \text{ s}^{-1}. \quad (24)$$

A comparison between the sfHO and the ffSC  $\text{N}_2$ - $\text{N}_2$  V-T rate coefficients together with the corresponding available semi-classical calculations [89, 90] (P. 104), [91] is presented in figure 3(a). A comparable  $k_{1,0}$  value is observed. However, at higher vibrational levels, the rate coefficients calculated with the ffSC are much larger than those calculated with the sfHO, e.g. around 6–8 orders of magnitude larger at  $v = 57$ . Note that the ffSC rate coefficients calculated from the fit function agree well with the aforementioned semi-classical calculations for  $v \leq 40$ . Furthermore, the  $\text{N}_2$ - $\text{N}_2$  V-T rate coefficients for  $v > 40$  calculated with the ffSC are observed to be close to those calculated with the SSH (not shown here). The roles of the sfHO and the ffSC V-T rate coefficients in the calculated whole  $\text{N}_2$  VDF evolution profiles are uncovered in section 5.3.

The rate coefficients  $k_{v,w}$  of the  $\text{N}_2$ - $\text{N}(^4\text{S})$  V-T reactions



are obtained with the following two approaches:

- (1) The sfHO  $k_{v,w}$  was calculated in [32] (P. 33):

$$k_{v,w} = v 4.0 \times 10^{-16} (T_g/300)^{1/2} \exp(-7062.76/T_g) \text{ m}^3 \text{ s}^{-1}, \quad v - w = 1 \text{ and } v \geq 1. \quad (26)$$

- (2) A fit function to the Quasi-Classical Trajectory (ffQCT) calculations was suggested by [77] (P. 12):

**Table 2.** Parameters, as a function of the gas temperature  $T_g$  in K, to be used in equation (27) for the rate coefficients of the  $\text{N}_2$ - $\text{N}(^4\text{S})$  V-T reactions.

	Reactive	Non-reactive
$A_0$	$0.2 \times 2.212 \times 10^{-12} / T_g^{1.426}$	$0.2 \times 9.240 \times 10^{-12} / T_g^{1.635}$
$A_1$	$3.210 \times 10^4 / T_g^{0.8147}$	$1.823 \times 10^4 / T_g^{0.6984}$
$A_2$	$2.521 \times 10^5 / T_g^{1.044}$	$9.893 \times 10^3 / T_g^{0.4376}$
$v^*$	7	9

$$k_{v,w} = A_0 \exp\left(-\frac{A_1}{v} + \frac{A_2}{v^2}\right) \text{ m}^3 \text{ s}^{-1}, \quad 1 \leq v - w \leq 5 \text{ and } v \geq v^*, \quad (27)$$

where the parameters  $A_0$ ,  $A_1$ ,  $A_2$  and  $v^*$  are provided in table 2. Both reactive and non-reactive collisions are incorporated. The former achieves an atomic exchange between  $\text{N}_2(v)$  and  $\text{N}(^4\text{S})$ , whereas the latter conducts a direct collision.

The deviation between the sfHO and the ffQCT  $\text{N}_2$ - $\text{N}(^4\text{S})$  V-T rate coefficients  $k_{v,w}$  at  $v - w = 1$  is shown in figure 3(b). The ffQCT  $k_{v,w}$  is smaller at low vibrational levels. However, they are larger than the sfHO  $k_{v,w}$  at high vibrational levels, where the V-T rate coefficients typically play a main role in shaping the VDF tail. The shaping ability of the ffQCT  $k_{v,w}$  to the VDF tail is enhanced by the combination of  $v - w = 1, 2, 3, 4, 5$ . A comparison between the  $\text{N}_2$  VDF evolution profiles calculated with the sfHO and the ffQCT is conducted in section 5.4.

#### 4.3. Backward reactions of the V-V and V-T kinetics

The backward reaction rate coefficients of the V-V and V-T kinetics presented in sections 4.1 and 4.2 are calculated from the forward ones based on detailed balance [77] (P. 11):

**Table 3.** A list of the theoretical approaches determining the V-V and V-T rate coefficients and the correspondingly used wall reaction probability  $\gamma$  of  $N_2(v) + \text{wall} \rightarrow N_2(v-1)$ . The  $N_2$ - $N_2$  V-V rate coefficient scaling laws: the sfHO, the SSH and the FHO are explained by equations (12), (16) and (17), respectively. The sfHO and ffSC approaches determining the  $N_2$ - $N_2$  V-T rate coefficients are given by equations (21) and (22), respectively. The sfHO and ffQCT  $N_2$ - $N(^4S)$  V-T rate coefficients are calculated by equations (26) and (27), respectively. The neutral wall reaction rate as a function of  $\gamma$  is provided by equation (6).

Section	$N_2$ - $N_2$ V-V	$N_2$ - $N_2$ V-T	$N_2$ - $N(^4S)$ V-T	$N_2(v) + \text{wall} \rightarrow N_2(v-1)$
Previous study [32]	sfHO	sfHO	sfHO	$\gamma = 1$
Section 5.1	sfHO/SSH/FHO	sfHO	sfHO	$\gamma = 3 \times 10^{-3}$
Section B	sfHO/SSH/FHO	sfHO	sfHO	$\gamma = 3 \times 10^{-3}$
Section 5.2	sfHO/SSH/FHO	sfHO	sfHO	$\gamma = 3 \times 10^{-3}$
Section 5.3	SSH	sfHO/ffSC	sfHO	$\gamma = 3 \times 10^{-3}$
Section 5.4	SSH	ffSC	sfHO/ffQCT	$\gamma = 3 \times 10^{-3}$
Section 5.5	SSH	ffSC	ffQCT	$\gamma = 3 \times 10^{-3}$
Section 5.6	SSH	ffSC	ffQCT	$\gamma = 0 - 1$

$$k_{v-1,v}^{w,w-1} = k_{v,v-1}^{w-1,w} \exp\left(\frac{\Delta E_{v,v-1}^{w-1,w}}{k_B T_g}\right), \quad (28)$$

$$k_{w,v} = k_{v,w} \exp\left(\frac{\Delta E_{v,w}}{k_B T_g}\right), \quad (29)$$

where  $\Delta E_{v,v-1}^{w-1,w} = E_{v-1} + E_w - E_v - E_{w-1} < 0$  and  $\Delta E_{v,w} = E_w - E_v < 0$ .

#### 4.4. Summary of the V-V and V-T kinetics calculation approaches used in the results section

The simple scaling law, the sfHO, was implemented for the nitrogen V-V and V-T kinetics in our previous study [32] to initially explore the role of the detailed vibrational kinetics in an atmospheric-pressure plasma jet. It was predicted [32] that the  $N_2$  VDF has an influence on the reactive neutral species densities. For example,  $N_2(v \geq 13)$  play a more important role in the NO formation at a higher power value in the range of 0.5 – 2 W of the COST-Jet [44]. In the wake of this prediction, several conventional theoretical approaches determining the V-V and V-T kinetics are incorporated in sections 5.1–5.4 and appendix B to further explore their influence on the validated electron density and  $N_2(v = 1, 2, 3, 4)$  densities as well as the simulated whole  $N_2$  VDF evolution profiles. Besides the sfHO implementation, other commonly used calculations of the  $N_2$ - $N_2$  V-V kinetics (i.e. the more sophisticated analytical approaches: the SSH and the FHO) are additionally implemented in sections 5.1, appendix B and 5.2. The simulation results using the sfHO V-T rate coefficients are compared with those using the more sophisticated theoretical approaches, i.e. compared with those using the ffSC  $N_2$ - $N_2$  V-T kinetics and the ffQCT  $N_2$ - $N(^4S)$  V-T mechanisms in sections 5.3 and 5.4, respectively. In the simulations of sections 5.2–5.6, the theoretical approaches determining the V-V and V-T rate coefficients are gradually implemented with the more sophisticated one (see table 3). Note that the SSH  $N_2$ - $N_2$  V-V rate coefficients are used in sections 5.3–5.6, since the SSH computations are similar to the FHO ones (both agreeing well with the semi-classical calculations of Billing and Fisher [89]) as shown in figures 2(a)–(c).

## 5. Results

### 5.1. Comparison between the simulations and measurements

The plasma jet simulated in this work is driven by three sets of DC ns-pulsed power as mentioned in section 2. The power-on phase in each set of power data consists of two parts: (i) a short period of high power deposition (around 25 ns) called peak-power phase, followed by (ii) a longer period of lower power deposition named plateau-power phase. The former plays an important role in the plasma ignition, whereas the latter maintains the discharge. The electron density (calculated based on experimental measurements) [29] and the measured ratios of the  $N_2(v = 1, 2, 3, 4)$  densities to the gas density [25] together with the 0-D simulation results from this work in the case of the above-mentioned three power sets are shown in figures 4, B1 and B2, respectively. The electron density calculated from the experimentally measured time-dependent current and the constant electric field is only evaluated during the plateau-power phase [29], and the absent density values during the peak-power phase and the power decay phase are ascribed to the sharply dynamic power resulting in a non-constant electric field. It should be emphasized that the sum of the  $N_2(v = 0 - 4)$  densities is accounted as the gas density in the measurement data, whereas the sum of the  $N_2(v = 0 - 57)$  densities is calculated as the gas density in the simulation results. The sum of the simulated  $N_2(v = 0 - 4)$  densities divided by that of the simulated  $N_2(v = 0 - 57)$  densities (even by that of all the included species densities) is greater than 99%. In other words, both the  $N_2(v = 0 - 4)$  densities and the  $N_2(v = 0 - 57)$  densities can be regarded as approximately equal to the gas density. Furthermore, the simulation results are calculated with three different theoretical approaches determining the  $N_2$ - $N_2$  V-V rate coefficients: i.e. the sfHO, the SSH and the FHO scaling laws explained in section 4.1. The  $N_2$ - $N_2$  and the  $N_2$ - $N(^4S)$  V-T kinetics used in the simulations in sections 5.1 and appendix B are calculated with the sfHO approach. For further details, see section 4.4.

The evolution of the power profile is nearly traced by that of both calculated electron density profiles in figure 4(a). The slower speed of the electron density decay compared to that of the power decay after the end of the plateau-power phase is

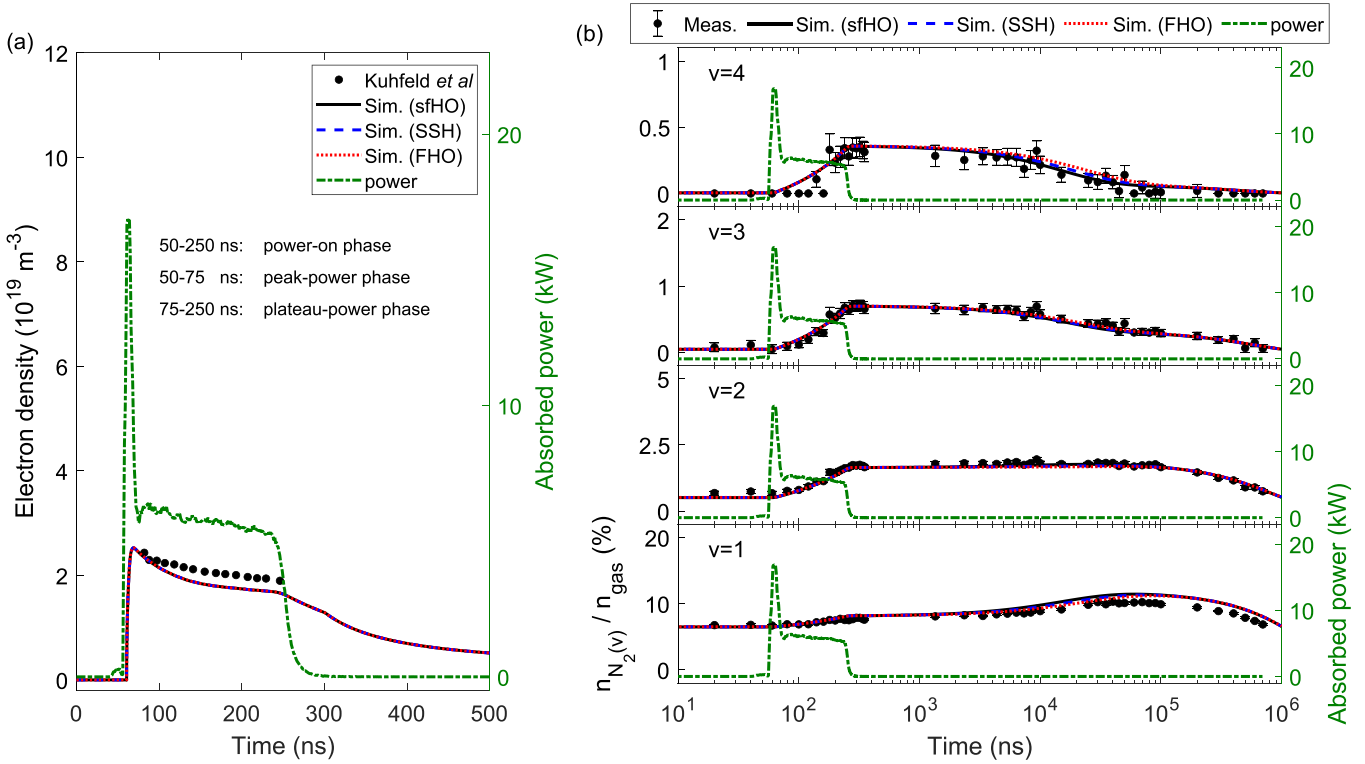


**Figure 4.** (a) Time-resolved electron density ( $\bullet$ ) calculated from the current and electric field measured by Kuhfeld *et al* [29]. (b) Time-resolved ratios of the nitrogen vibrational level densities  $n_{N_2(v=1,2,3,4)}$  to the gas density  $n_{\text{gas}}$  measured by Kuhfeld *et al* [25] ( $\bullet$ ). The electron density and the density ratios are calculated by the 0-D model using the  $N_2$ - $N_2$  V-V rate coefficient scaling laws of the sfHO (—), the SSH (---) and the FHO (.....) (see section 4.1). The  $N_2$ - $N_2$  and the  $N_2$ - $N(^4S)$  V-T kinetics are calculated with the sfHO approach (see section 4.4). For the sake of clarity, the evolution of the electron density is shown only during the power-on phase, whereas that of the density ratios is presented inside one pulse period. 200 ns power-on duration and 17 kW peak power value in a 1 kHz modulation period (---, i.e. the absorbed power in the whole plasma volume) are used to drive the  $1 \times 1 \times 20 \text{ mm}^3$  plasma domain at a gas temperature of around 330 K. 20 sccm  $N_2$  are fed to the chamber at a pressure of 20 000 Pa. For further details of the operating conditions, see section 2.

controlled by reaction 22 in table A1:  $e + N_4^+ \rightarrow 2 N_2(v=0)$ . Comparable electron density values are observed in the calculation of [29] (based on the measured current and electric field) and in our 0-D simulation result. These values were also reported in [52, 53]. Similar electron density values are obtained from the 0-D simulation results adopting the above-mentioned three different V-V rate coefficient scaling laws. In addition, the evolution of the measured and simulated ratios of the  $N_2(v=1,2,3,4)$  densities to the gas density within a pulse modulation cycle as shown in figure 4(b) are also similar for each V-V rate coefficient scaling law. The  $N_2(v=1,2,3,4)$  densities are increased throughout the power-on duration as a result of energy transfer from the absorbed power to the vibrational excitation (by electron-impact excitation of vibrational levels, i.e. the e-V kinetics). The increased  $N_2(v=1,2,3,4)$  densities in the plateau-power phase are partially contributed by the V-V up-pumping. This partial contribution is ascribed to the growing vibrational level densities in this duration relative to those in the peak-power phase, see equation (3). In contrast to the power-on phase, the  $N_2(v=1,2,3,4)$  densities are reduced in the afterglow due to the absence of external energy support, and the V-V mechanisms are observed to play a major role to shape the presented evolution profiles. A slow increase of the  $N_2(v=1)$  density in the

afterglow is mainly controlled by the dominant  $N_2(v=1)$  production and destruction mechanisms: i.e. the backward and forward reactions of  $N_2(v=1) + N_2(v=1) \leftrightarrow N_2(v=0) + N_2(v=2)$ , respectively. Both reactions provide around 55%—85% of the  $N_2(v=1)$  production and destruction during  $1 \times 10^3$ – $1 \times 10^5$  ns. In this duration, it is hinted in figure 4(b) that  $n_{N_2(v=1)}n_{N_2(v=1)} < n_{N_2(v=0)}n_{N_2(v=2)}$ , and it is further calculated that  $k_{1,0}^{1,2}n_{N_2(v=1)}n_{N_2(v=1)} < k_{2,1}^{0,1}n_{N_2(v=0)}n_{N_2(v=2)}$ , see equations (3) and (28). In other words, the reaction rate of the aforementioned backward reaction is greater than that of the forward reaction, and this leads to the  $N_2(v=1)$  density increased during  $1 \times 10^3$ – $1 \times 10^5$  ns. The  $N_2(v=1)$  density well-validated between the measurements and the simulations in the whole modulation cycle implies that the backward reactions play a non-negligible role in the V-V kinetics.

Nearly identical evolution of the ratios of the  $N_2(v=1,2,3,4)$  densities to the gas density are captured by the simulation results using the sfHO, the SSH and the FHO scaling laws, as shown in figure 4(b). This is consistent with the V-V rate coefficients presented in figures 2(a) and (d), i.e.  $k_{1,0}^{v-1,v}$  and  $k_{v,v-1}^{v,v+1}$  calculated where the rate coefficients determined from the aforementioned three scaling laws are comparable for cases where  $v < 5$ . The above-mentioned outcomes are likewise obtained in the simulation results considering an

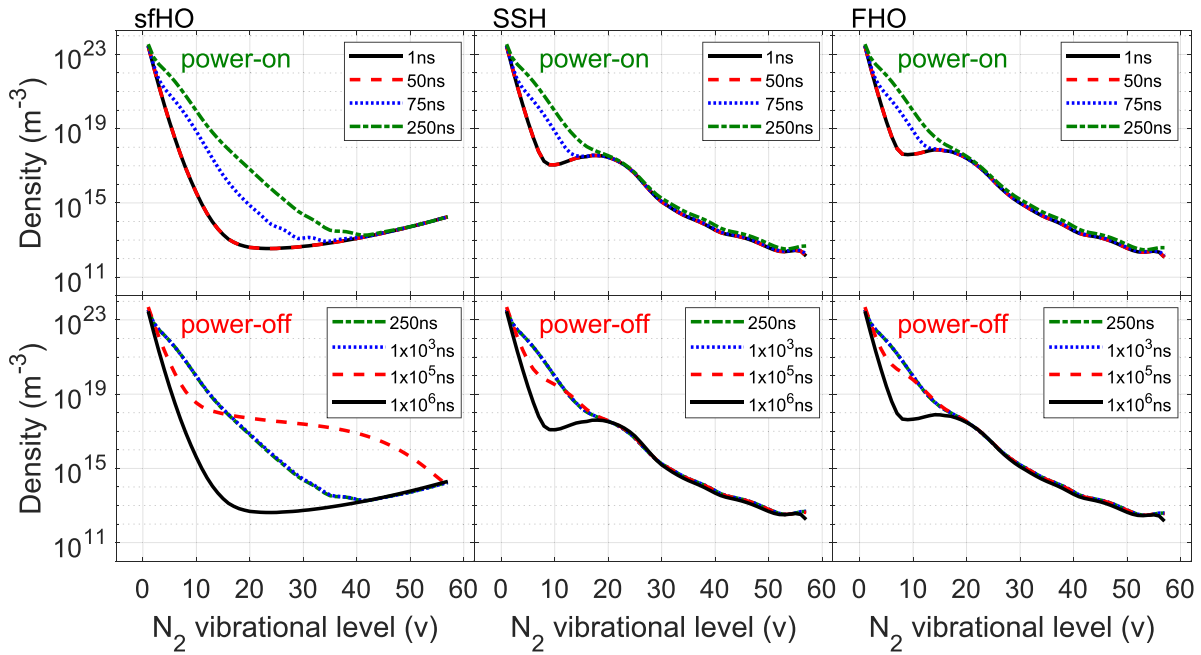


**Figure 5.** Time-dependent evolution of  $N_2$  VDFs calculated with the  $N_2$ - $N_2$  V-V rate coefficient scaling laws of the sfHO, the SSH and the FHO (see section 4.1). The  $N_2$ - $N_2$  and the  $N_2$ - $N(^4S)$  V-T kinetics are calculated with the sfHO approach (see section 4.4). The VDF evolution is presented during the power-on (50–250 ns) and the power-off (250– $1 \times 10^6$  ns). The operating conditions are identical to those in figure 4.

increase of the power-on duration and peak power value in figures B1 and B2, respectively. The  $N_2(v = 1, 2, 3, 4)$  densities inside one modulation period are overall elevated with these two increasing operating parameters due to the growing energy per pulse.

### 5.2. Role of $N_2$ - $N_2$ V-V rate coefficients in the calculated VDFs

The  $N_2$  VDFs calculated with the sfHO, the SSH and the FHO V-V rate coefficients are provided in figure 5. The  $N_2$ - $N_2$  and the  $N_2$ - $N(^4S)$  V-T kinetics used in the simulations in section 5.2 are calculated with the sfHO approach. For further details, see section 4.4. The VDF evolution inside one modulation period (0– $1 \times 10^6$  ns) is divided into two phases: the power-on (50–250 ns) and the power-off (250– $1 \times 10^6$  ns). During the power-on, the peak-power phase (50–75 ns) and the plateau-power phase (75–250 ns) are presented to investigate their influence on the VDF evolution. For the sake of clarity in the power-off phase, the evolution of the VDFs is reported only at four time points in different orders of magnitude: i.e. 250 ns,  $1 \times 10^3$  ns,  $1 \times 10^5$  ns and  $1 \times 10^6$  ns. As expected, the vibrational level densities are continuously enhanced during the peak- and plateau-power phases, and the main contribution to the enhanced absolute densities is from the latter. In the simulation results using the sfHO, the SSH and the FHO, similar evolution of the  $N_2(v < 5)$  densities is observed in the whole modulation period, as also observed in figure 4(b).

In figure 5, the VDF( $v \geq 5$ ) evolution calculated with the sfHO strongly differs from those calculated with the SSH and the FHO. Smaller intermediate vibrational level densities

(about  $10 \leq v < 40$  for here) and larger high level densities (about  $v \geq 40$  for here) are achieved in the case of the sfHO implementation. This possibly overestimated VDF tail is consistent with the observation that the V-V rate coefficients reported in figures 2(a)–(c), i.e.  $k_{1,0}^{v-1,v}$ ,  $k_{6,5}^{v-1,v}$  and  $k_{11,10}^{v-1,v}$  calculated with the sfHO are larger than those calculated with the SSH and the FHO especially at higher vibrational levels. In other words, the lower vibrational level densities are up-pumped to the higher level region through the excessive sfHO V-V rate coefficients. This up-pumping effect is more noticeable in the power-off phase, where at  $1 \times 10^5$  ns, even larger intermediate vibrational level densities are achieved in the case of the sfHO implementation relative to the SSH and the FHO. As a result of this noticeable up-pumping effect in the power-off phase, the dominant gain and loss mechanisms of the high vibrational levels under the sfHO implementation are provided by the V-V kinetics. Those under the SSH and the FHO implementation are controlled by the wall quenching effect of these high vibrational levels.

Similar evolution is given between the VDF calculated by the SSH and the FHO in figure 5. This is attributed to the similar V-V rate coefficients calculated by both approaches, see figures 2(a)–(c). Both calculations provide a dynamic (time-variant)  $N_2(v < 20)$  density distribution and a stable (time-invariant)  $N_2(v \geq 20)$  concentration profile over the whole pulse period. During the power-on phase, the e-V kinetics play a main role in the production of the vibrational levels. Larger production rates are predicted for lower levels. This likely results in the increased  $N_2(v < 20)$  (low levels) densities and the stable  $N_2(v \geq 20)$  (high levels) concentrations during the power-on phase. During the power-off phase, the V-V kinetics

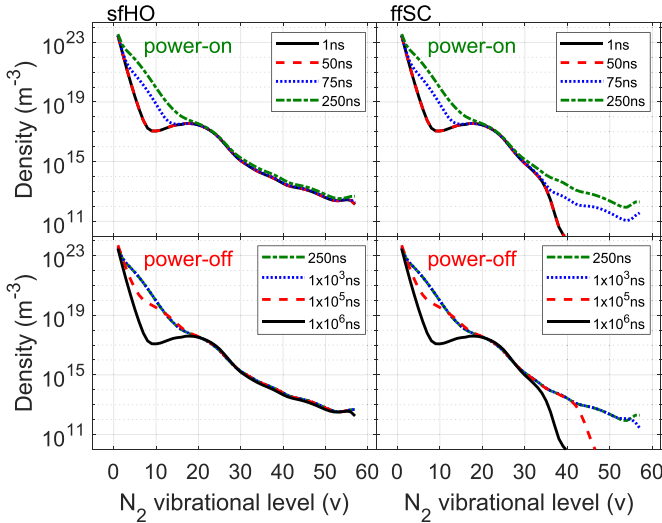


**Figure 6.** Time-dependent evolution of  $N_2$  VDFs calculated with the  $N_2$ - $N_2$  V-T rate coefficient scaling laws of the sfHO and of the ffSC (see section 4.2). The  $N_2$ - $N_2$  V-V kinetics are calculated with the SSH approach, and the  $N_2$ - $N(^4S)$  V-T kinetics are calculated with the sfHO approach (see section 4.4). The VDF evolution is presented during the power-on (50–250 ns) and the power-off (250– $1 \times 10^6$  ns). The operating conditions are identical to those in figure 4.

have a key influence on the shape of the VDF profiles, e.g. it is found that the SSH and FHO V-V rate coefficients  $k_{1,0}^{v-1,v}$  shown in figure 2(a) have a non-negligible influence on the production and destruction of  $N_2(v=4)$  and  $N_2(v=25)$ . Note that the peak values of the SSH and FHO  $k_{1,0}^{v-1,v}$  are around in the region of  $5 < v < 10$ . This likely leads to the significantly reduced  $N_2(5 < v < 10)$  densities during the power-off phase. The populations of these states are transferred to higher vibrational levels though the V-V kinetics i.e. vibrational up-pumping. Consequently, a local minimum density at around  $v=9$  and a local maximum density at around  $v=17$  are obtained. The  $N_2(v \geq 20)$  concentrations are stable during the power-off phase. This is likely due to smaller up-pumping effect of the SSH and FHO V-V rate coefficients at higher vibrational level (relative to the sfHO ones), see figures 2(a)–(c). Furthermore, the quenching effect of the sfHO V-T rate coefficients at high vibrational level is also small (relative to the ffSC and ffQCT ones), see figures 3(a) and (b). These up-pumping and quenching effects have a negligible influence on the production and destruction of the high vibrational levels. A Maxwellian-like distribution function is observed among the stable  $N_2(v \geq 20)$  concentrations.

### 5.3. Role of $N_2$ - $N_2$ V-T rate coefficients in the calculated VDFs

The  $N_2$  VDFs calculated with the  $N_2$ - $N_2$  V-T rate coefficient scaling laws of the sfHO and of the ffSC are reported in figure 6. In the simulations in section 5.3, The  $N_2$ - $N_2$  V-V kinetics are calculated with the SSH approach, and the  $N_2$ - $N(^4S)$  V-T kinetics are calculated with the sfHO approach. For further details, see section 4.4. The evolution of the VDFs

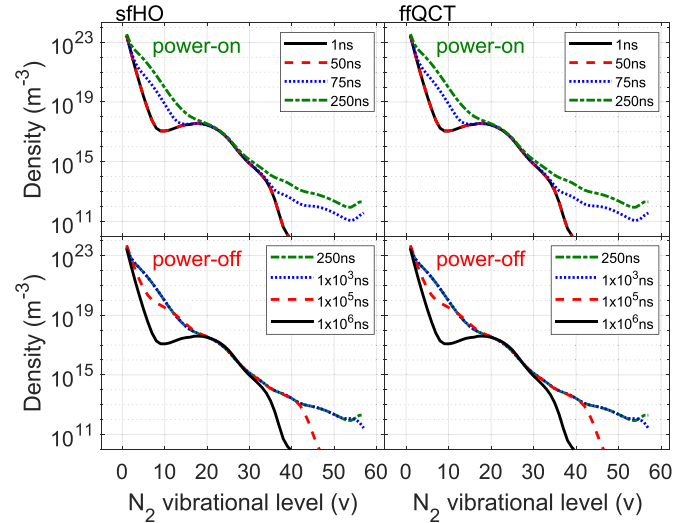


**Figure 7.** Time-dependent evolution of  $N_2$  VDFs calculated with the sfHO and ffQCT  $N_2$ - $N(^4S)$  V-T rate coefficients (see section 4.2). The  $N_2$ - $N_2$  V-V kinetics are calculated with the SSH approach, and the  $N_2$ - $N_2$  V-T kinetics are calculated with the ffSC approach (see section 4.4). The VDF evolution is presented during the power-on (50–250 ns) and the power-off (250– $1 \times 10^6$  ns). The operating conditions are identical to those in figure 4.

in the power-on and power-off phases inside one modulation period is presented in a same way as that in figure 5. A practically equivalent  $N_2(v < 30)$  density profile is observed in the simulation results using both scaling laws. However, a more significant distinction is shown in the concentrations of higher vibrational levels, i.e. the  $N_2(v \geq 30)$  densities calculated with the sfHO are stable and present a Maxwellian-like distribution during the whole modulation period, whereas those calculated with the ffSC are dynamic. In the power-on phase, the dynamic  $N_2(v \geq 30)$  densities are stepwise increased during the peak- and plateau-power phase, and increased by up to one order of magnitude in the latter. In the power-off phase, the  $N_2(v \geq 30)$  densities drop starting from higher vibrational levels, e.g. the relaxation of the  $N_2(v=55)$  density starts at  $1 \times 10^3$  ns and that of the  $N_2(v=42)$  concentration starts at  $1 \times 10^5$  ns. The dynamic behaviour of the  $N_2(v \geq 30)$  densities is ascribed to the much larger ffSC V-T rate coefficients than the sfHO ones at higher vibrational levels, as presented in figure 3(a). As a result, the high vibrational level densities calculated with the ffSC are overall smaller than those calculated with the sfHO, especially at the end of the power-off phase. The simulated dynamics of the  $N_2(30 \leq v \leq 40)$  densities are potentially more reliable than the simulated dynamics of the  $N_2(v > 40)$  densities, since the ffSC rate coefficients agree well with the corresponding semi-classical calculations for  $v \leq 40$ , see section 4.2.

### 5.4. Role of $N_2$ - $N(^4S)$ V-T rate coefficients in the calculated VDFs

The  $N_2$  VDF evolution profiles calculated with the sfHO and ffQCT  $N_2$ - $N(^4S)$  V-T rate coefficients are shown in figure 7. In the simulations in section 5.4, the  $N_2$ - $N_2$  V-V kinetics are

calculated with the SSH approach, and the  $N_2$ - $N_2$  V-T kinetics are calculated with the ffSC approach. For further details, see section 4.4. The temporal evolution profiles are presented in the same way as those in figure 5. Identical evolution profiles over the whole pulse period are obtained between the VDFs calculated with the sfHO and the ffQCT. Note that the  $N_2$ - $N(^4S)$  V-T rate coefficients of the ffQCT are much larger than those of the sfHO in the intermediate and high vibrational level region, see figure 3(b). The identical evolution profiles of the VDFs calculated with the sfHO and the ffQCT are still obtained. The negligible influence of the ffQCT  $N_2$ - $N(^4S)$  V-T rate coefficients on the intermediate and high vibrational level densities at near atmospheric pressure and room temperature is ascribed to two points: (i) the  $N_2(v=0)$  density is at least three orders of magnitude larger than the  $N(^4S)$  density over the whole modulation cycle, and (ii) the V-T rate coefficient values of the ffSC  $N_2$ - $N_2$  are smaller than those of the ffQCT  $N_2$ - $N(^4S)$  in the range of  $v \geq 30$  (but at most 1 order of magnitude smaller) as presented in figure 3. In other words, at near atmospheric pressure and room temperature, the quenching reaction rates of the ffSC  $N_2$ - $N_2$  V-T kinetics are much larger than those of the ffQCT  $N_2$ - $N(^4S)$  V-T mechanisms, see equation (3). Consequently, the ffSC  $N_2$ - $N_2$  V-T channels play a major role in shaping the VDF tails. Potentially larger  $N(^4S)$  density (i.e. the  $N_2$  discharge with higher dissociation degree) might be achieved with a different operating condition compared to this work. This might increase the quenching reaction rates of the ffQCT  $N_2$ - $N(^4S)$  V-T mechanisms, and further increase the role of the ffQCT  $N_2$ - $N(^4S)$  V-T channels in shaping the VDF profile. It is worth to note that the larger  $N_2$ - $N(^4S)$  V-T rate coefficients provided by Capitelli *et al* [83] and Esposito *et al* [92] in comparison with those provided by the ffQCT shown in [77] might further diminish the overall population on the  $N_2$  VDF tails.

##### 5.5. Effect of including different numbers of vibrational levels

The variation of the VDF evolution is simulated for varying numbers of vibrational levels considered in the 0-D model: i.e.  $N_2(v < 58)$ ,  $N_2(v < 41)$  and  $N_2(v < 7)$ . In the simulations in section 5.5, the  $N_2$ - $N_2$  V-V, the  $N_2$ - $N_2$  V-T and the  $N_2$ - $N(^4S)$  V-T kinetics are calculated with the SSH, the ffSC and the ffQCT approaches, respectively. For further details, see section 4.4. Identical evolution is observed regarding the electron density and the ratios of the  $N_2(v = 1, 2, 3, 4)$  densities to the gas density in the simulation results considering the aforementioned varying numbers of vibrational levels. In other words, the measurements shown in figure 4 are already captured by the simulations considering a simple chemistry model with  $N_2(v < 7)$ . Furthermore, nearly identical VDF evolution profiles are found between the simulation results considering  $N_2(v < 41)$  and  $N_2(v < 58)$ . Therefore, the relevant simulation results are not depicted in this paper. Note that the elevated last few vibrational level densities during the power-on phase shown in the simulation results considering  $N_2(v < 58)$  (e.g. the upward  $N_2(54 < v < 58)$  densities from 75 ns to 250 ns in figure 7) are not observed in the simulation results considering  $N_2(v < 41)$  (i.e. the upward  $N_2(37 < v < 41)$  densities are

not observed). A test has been carried out that such an elevation during the power-on phase, where e-V kinetics play a main role, is not predicted in the simulation results considering  $N_2(v < 55)$ , where  $v = 55$  is considered as a pseudo level. Therefore, this elevation is not associated with the description of dissociation from the last vibrational level, but it is likely due to the used data of the e-V kinetics under the current operating conditions.

##### 5.6. Role of vibrational de-excitation at surfaces

The modification of the  $N_2$  VDF evolution within one pulse modulation period by varying the considered wall reaction probabilities  $\gamma$  between 0 and 1 is simulated by the 0-D model, see equation (6). In the simulations in section 5.6, the  $N_2$ - $N_2$  V-V, the  $N_2$ - $N_2$  V-T and the  $N_2$ - $N(^4S)$  V-T kinetics are calculated with the SSH, the ffSC and the ffQCT approaches, respectively. For further details, see section 4.4. The electron density is barely affected by any included neutral wall reaction. It is found that the  $N_2$  VDF evolution is not sensitive to any included wall quenching of the electronically excited state and the wall recombination of the nitrogen atom. However, a significant influence of the  $N_2(0 < v < 58)$  wall quenching on the  $N_2$  VDF evolution is seen in figure 8. As  $\gamma$  of  $N_2(v) + \text{wall} \rightarrow N_2(v-1)$  is changed from 1 to 0, the  $N_2(0 < v < 58)$  densities are remarkably enhanced especially those in the intermediate vibrational level region, e.g. the enhanced  $N_2(10 < v < 30)$  densities are located in a range between  $1 \times 10^{19} \text{ m}^{-3}$  and  $1 \times 10^{21} \text{ m}^{-3}$  during the whole modulation period for the case  $\gamma = 0$ . As noted earlier in section 3, all the results in section 5 and appendix B are obtained from the simulations of nitrogen plasma under 6 pulses (based on the calculated residence time of the feed gas in the jet chamber, see section 3). The simulation results at  $\gamma = 0$  do not yet reach the periodic steady state, and therefore much larger intermediate vibrational level densities are expected for a longer residence time.

The  $N_2(0 < v < 58)$  densities are overall enhanced whereas the  $N_2(v=0)$  density is reduced by a factor of around 1.3 due to the variation of  $\gamma$  from 1 to 0. In the wake of this variation, due to the changed plasma composition (e.g. the enhanced VDF population) and the following complex chemical kinetics, the simulated effective electron temperature is increased around 0.2 eV in the plateau-power phase which facilitates a higher contribution from the e-V kinetics to enhance the absolute densities of the  $N_2(0 < v < 58)$  levels in this phase. Both the reduced background gas density and the increased effective electron temperature imply that a more efficient vibrational excitation is likely achieved by smaller  $N_2(0 < v < 58)$  wall quenching probabilities (depending on the surface conditions), since the applied power is the same for both  $\gamma = 1$  and  $\gamma = 0$  in figure 8. Note that the ratios of the  $N_2(v = 1, 2, 3, 4)$  densities to the gas density in the case of the reference value  $\gamma = 3 \times 10^{-3}$  are validated in figure 4(b), whereas those in the case of  $\gamma = 0$  or 1 are problematic: i.e. the simulated ratios either overestimate or underestimate the measurement data around by a factor of 1 – 4, and the temporal evolution profiles of the simulations can not well capture those of the measurements, see figure 9(a).

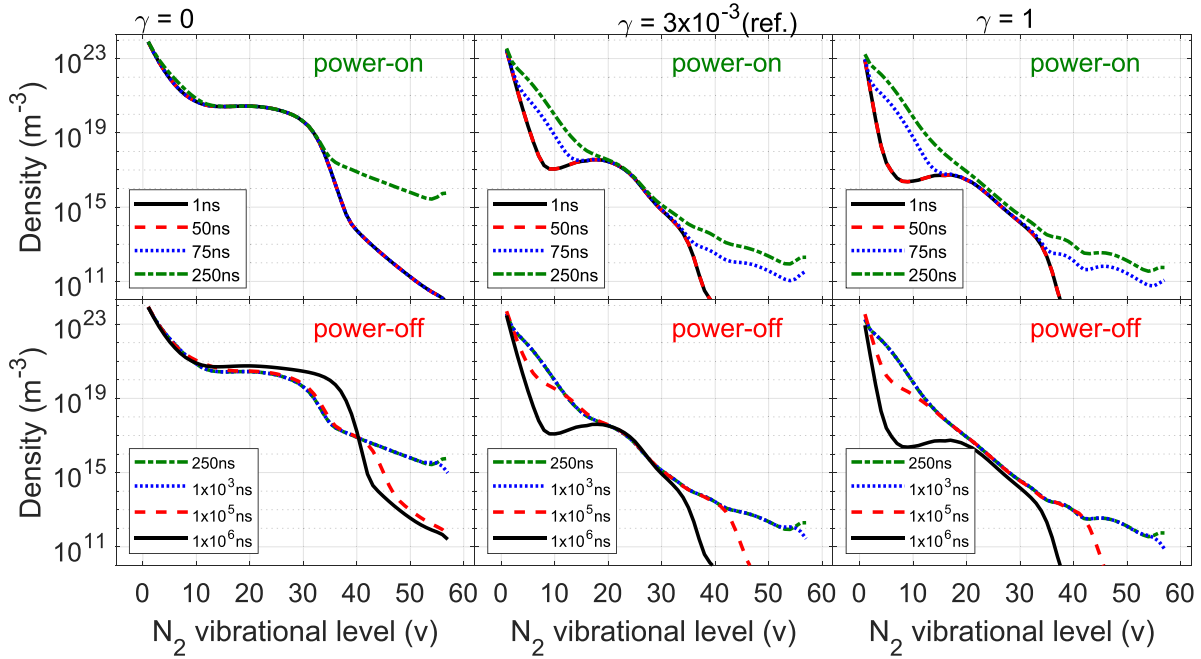


**Figure 8.** Time-dependent evolution of  $N_2$  VDFs calculated with the wall reaction probability  $\gamma = 0$ ,  $3 \times 10^{-3}$  (the reference value) and 1 of  $N_2(v) + \text{wall} \rightarrow N_2(v-1)$ , see equation (6). The  $N_2$ - $N_2$  V-V, the  $N_2$ - $N_2$  V-T and the  $N_2$ - $N(^4S)$  V-T kinetics are calculated with the SSH, the ffSC and the ffQCT approaches, respectively (see section 4.4). The VDF evolution is presented during the power-on (50–250 ns) and the power-off (250– $1 \times 10^6$  ns). The operating conditions are identical to those in figure 4.

It should be emphasized that the aforementioned enhanced VDF population in the simulations due to a variation of  $\gamma$  from 1 to 0 is mainly achieved by that from  $1 \times 10^{-2}$  to  $1 \times 10^{-4}$ . The reference value  $\gamma = 3 \times 10^{-3}$  adopted from an experimental work [74] (see notes in table A4) is located in the range of  $1 \times 10^{-2}$ – $1 \times 10^{-4}$ . In other words, the simulated VDF evolution profiles are sensitive to the adopted  $N_2(0 < v < 58)$  wall quenching probabilities. It is confirmed that the agreement between the simulated and measured ratios of the  $N_2(v = 1, 2, 3, 4)$  densities to the gas density in figure 4(b) is weakened, in case that the reference value  $\gamma = 3 \times 10^{-3}$  is increased or decreased over a factor of 2 in the simulations, see figure 9(b). More accurate  $N_2(0 < v < 58)$  wall quenching probabilities are of importance for a more reliable VDF prediction.

Additional simulations considering two alternative assumptions of the  $N_2(0 < v < 58)$  wall quenching are conducted in this work in order to further explore the sensitivity of the simulated VDFs to the  $N_2(0 < v < 58)$  wall quenching. The first assumption is that the constant wall reaction probability  $\gamma = 3 \times 10^{-3}$  of  $N_2(v) + \text{wall} \rightarrow N_2(v-1)$  is replaced by  $\gamma = 3 \times 10^{-3} v$  as a function of the vibrational level number  $v$  for a sensitivity analysis in the simulations. The same electron density and ratios of the  $N_2(v = 1, 2, 3, 4)$  densities to the gas density are obtained between the simulation results using  $\gamma = 3 \times 10^{-3}$  and  $\gamma = 3 \times 10^{-3} v$  (both agreeing well with the measurement data and simulation results shown in figure 4). The  $N_2(0 < v < 58)$  densities in the simulation results considering  $\gamma = 3 \times 10^{-3} v$  are smaller than those considering  $\gamma = 3 \times 10^{-3}$  (at the provided time points in figure 8) by a factor of 1.0–3.9. The second assumption is

that  $N_2(v) + \text{wall} \rightarrow N_2(v-1)$  is replaced by another form of the wall quenching  $N_2(v) + \text{wall} \rightarrow N_2(v=0)$  with the reference wall reaction probability  $\gamma = 3 \times 10^{-3}$  for a sensitivity analysis in the simulations. Almost identical electron density and ratios of the  $N_2(v = 1, 2, 3, 4)$  densities to the gas density are obtained between the simulation results considering the aforementioned two reaction forms (both agreeing well with the measurement data and simulation results shown in figure 4). The  $N_2(0 < v < 58)$  densities in the simulation results considering  $N_2(v) + \text{wall} \rightarrow N_2(v=0)$  are smaller than those considering  $N_2(v) + \text{wall} \rightarrow N_2(v-1)$  (at the provided time points in figure 8) by a factor of 1.0–5.3. It is worth to note that comparable evolution of the whole VDF profiles is obtained between the simulation results considering the above-mentioned two different wall reaction probability values or two different reaction forms (not shown here).

## 6. Conclusion

A transient 0-D volume-averaged model is developed to study a DC ns-pulsed plasma jet fed with  $N_2$  at near atmospheric pressure. The model is coupled with a Boltzmann solver (LoKI-B) under the two-term approximation for a self-consistent description of the electron kinetics. In the case of the DC pulses, the voltage drop is mainly applied to the powered electrode of the two planar electrodes in the plasma jet. It was recently reported that merely a part of the plasma volume (specifically, 80% volume of the  $N_2$  discharge) on the side of the grounded electrode is a homogeneous region [25, 52, 53], and around 35% of the total absorbed power is distributed into

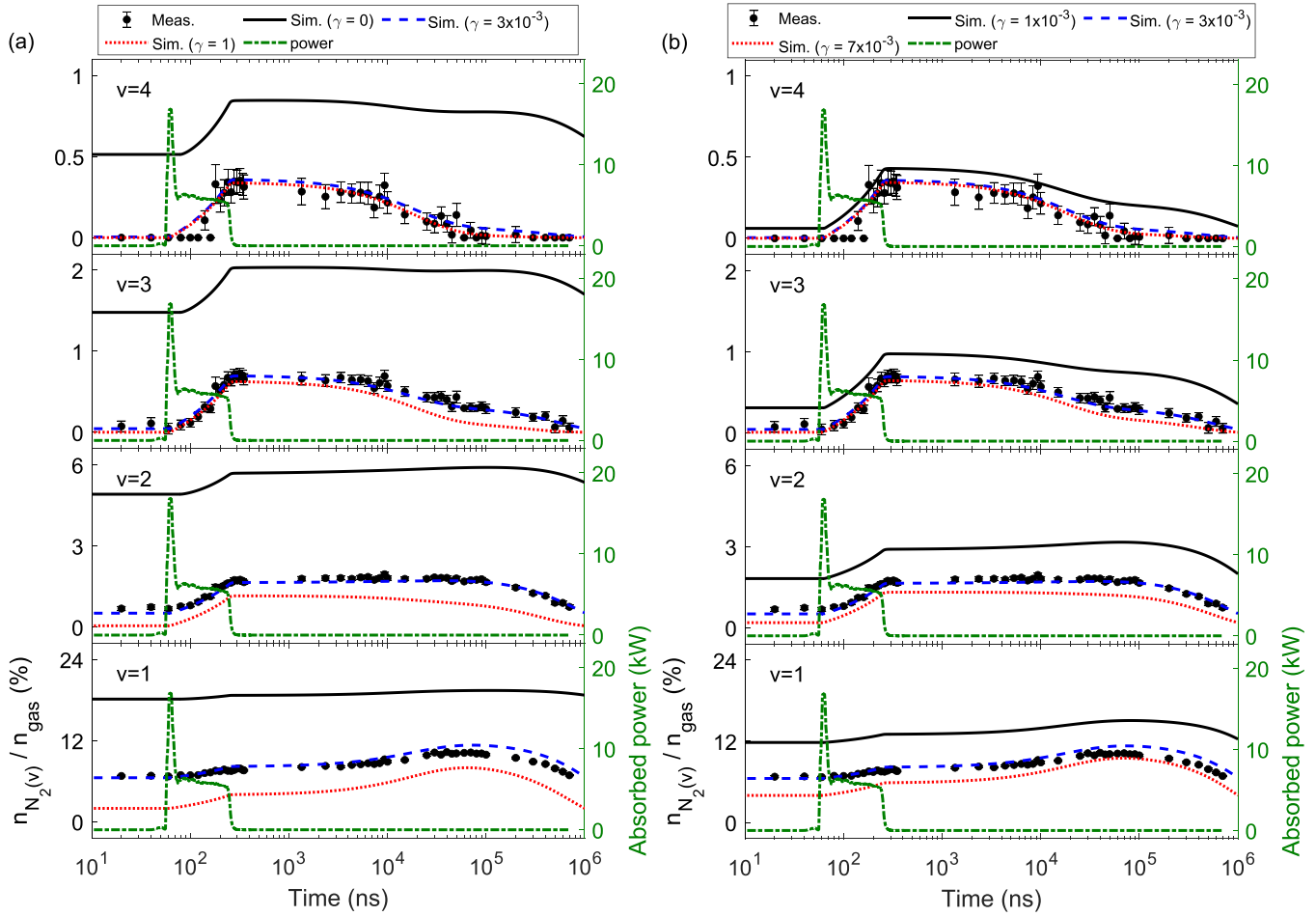


**Figure 9.** Time-resolved ratios of the nitrogen vibrational level densities  $n_{N_2(v)}$  ( $v=1,2,3,4$ ) to the gas density  $n_{\text{gas}}$  measured by Kuhfeld *et al* [25] ( $\bullet$ ), and calculated by the 0-D model considering  $N_2(v) + \text{wall} \rightarrow N_2(v-1)$  with the wall reaction probability (a)  $\gamma = 0$  (—),  $\gamma = 3 \times 10^{-3}$  (- - -), i.e. the reference value and  $\gamma = 1$  (· · · ·) and with the wall reaction probability (b)  $\gamma = 1 \times 10^{-3}$  (—),  $\gamma = 3 \times 10^{-3}$  (- - -), i.e. the reference value and  $\gamma = 7 \times 10^{-3}$  (· · · ·), see equation (6). The  $N_2$ - $N_2$  V-V, the  $N_2$ - $N_2$  V-T and the  $N_2$ - $N(^4S)$  V-T kinetics are calculated with the SSH, the ffSC and the ffQCT approaches, respectively (see section 4.4). The evolution of the density ratios is presented inside one pulse period. The operating conditions are identical to those in figure 4.

this region [25]. Since the measurements shown in this work were conducted in this homogeneous region, the corresponding absorbed power density value in this region is used in our 0-D model calculations in order to achieve a reasonable validation between the experiments and simulations. Our simulation results are compared well with the measurement data [25, 29]: including the electron density and the ratios of the  $N_2(v = 1, 2, 3, 4)$  densities to the gas density.

The ns-pulsed  $N_2$  plasma is investigated with a focus on the influence of the V-V and V-T kinetics on the temporal evolution of the VDFs within one pulse modulation cycle. The  $N_2$ - $N_2$  V-V rate coefficients are calculated from diverse theoretical approaches: including the sfHO, the SSH and the FHO. The V-V rate coefficients calculated from the sfHO are larger than those calculated from the SSH and the FHO especially at higher vibrational levels. It is observed that the time-dependent VDFs ( $v < 5$ ) are not affected by the aforementioned different approaches. However, a strongly different evolution is presented by the VDFs ( $v \geq 5$ ) calculated with the sfHO in comparison with the SSH and the FHO, e.g. larger high vibrational

level densities are obtained in the case of the sfHO implementation due to its excessive up-pumping effect. It is shown that similar evolution profiles are provided between the VDFs calculated with the SSH and the FHO, attributed to the nearly identical V-V rate coefficients calculated by both approaches. The  $N_2$ - $N_2$  V-T rate coefficients are determined by the sfHO and the ffSC, and significantly reduced VDFs ( $v \geq 30$ ) in the afterglow are acquired by the simulation results using the ffSC relative to using the sfHO. The  $N_2$ - $N(^4S)$  V-T rate coefficients are defined by the sfHO and the ffQCT, and a negligible difference of the VDF evolution is reported by the simulations using both approaches (since the  $N(^4S)$  density under the operating conditions in this study is at least three orders of magnitude smaller than the  $N_2(v = 0)$  density during the whole pulse period). However, in the case of larger  $N(^4S)$  density under a different operating condition compared to this study, the ffQCT  $N_2$ - $N(^4S)$  V-T kinetics might play a role in shaping the VDF profiles.

In accordance with the simulation results of the DC ns-pulsed  $N_2$  plasma in this study, the V-V and V-T kinetics

are recommended as follows. In the case of only considering  $N_2(v < 5)$  in the chemical model, the simulation results using the sfHO V-V and V-T kinetics as simple approaches can already well describe the transient behaviour of the measured  $N_2(v < 5)$  densities. In the case of considering  $N_2(v \geq 5)$ , the SSH and FHO  $N_2$ - $N_2$  V-V and ffSC  $N_2$ - $N_2$  V-T rate coefficients are recommended, since they agree well with the comprehensive and reliable data of the semi-classical calculations for  $v \leq 40$ . Moreover, the ffQCT  $N_2$ - $N(^4S)$  V-T kinetics are recommended in the simulations of the  $N_2$  plasma with high dissociation degree due to their potential influence on the high vibrational level densities. Note that the simulation results using these V-V and V-T kinetics recommended in the case of considering  $N_2(v \geq 5)$  also well capture the measured  $N_2(v < 5)$  densities. It should be emphasized that in principle the accuracy of these V-V and V-T kinetics could be further confirmed by the validation between the simulated and measured  $N_2(v \geq 5)$  densities, e.g. the accuracy of the ffSC  $N_2$ - $N_2$  V-T rate coefficients in terms of their significant influence on the  $N_2(v \geq 30)$  densities. However, such a validation is currently not accessible due to the weaker signal in the measurements of higher vibrational level densities. A further optimization for the accurate measurement of the high vibrational level densities is essential for the accurate prediction of the whole VDF evolution profiles.

The sensitivity of the simulated VDF evolution to the variation of the total number of vibrational levels considered in the simulations and to the variation of the wall reaction probabilities considered in the chemical model is analysed. It is found that the measurements are already captured by the simulations considering a limited set of vibrational levels: i.e.  $N_2(v < 7)$ . It is indicated that the neutral wall reaction probabilities of  $N_2(v) + \text{wall} \rightarrow N_2(v - 1)$  play a significant role in the evolution of the VDFs. The simulated VDFs especially at

intermediate and high vibrational levels are overall enhanced by reducing the wall quenching probabilities of  $N_2(v < 58)$  from the reference value  $3 \times 10^{-3}$  to 0. Nevertheless, the achieved agreement between the measured and simulated ratios of the  $N_2(v = 1, 2, 3, 4)$  densities to the gas density is destroyed by this reduction. Furthermore, the reference value  $3 \times 10^{-3}$  is located in the range of  $1 \times 10^{-2}$  to  $1 \times 10^{-4}$  where the simulated ratios and VDF evolution profiles are strongly sensitive to the  $N_2(v < 58)$  wall quenching probabilities. A further analysis of these probabilities is of importance for a more accurate prediction of the VDFs, e.g. a analysis for the wall reaction probabilities of each vibrational level under the specific operating conditions and the corresponding wall surface status.

### Data availability statement

The data that support the findings of this study will be made openly available on the database <https://rdpcidat.rub.de/>.

### Acknowledgments

Funded by the Deutsche Forschungsgemeinschaft (DFG, German Research Foundation)—Project Number 327886311 (SFB 1316: A9, A2 and A1). IPFN activities were supported by FCT-Fundação para a Ciência e Tecnologia under Projects UIDB/50010/2020 (<https://doi.org/10.54499/UIDB/50010/2020>), UIDP/50010/2020 (<https://doi.org/10.54499/UIDP/50010/2020>), LA/P/0061/202 (<https://doi.org/10.54499/LA/P/0061/2020>) and PTDC/FIS-PLA/1616/2021 (<https://doi.org/10.54499/PTDC/FIS-PLA/1616/2021>). The authors are indebted to Dr Helen Davies for discussions on the nitrogen vibrational kinetics.

Appendix

Appendix A. Chemical kinetics included in this work together with the updates and supplements compared to those in our previous work [32]

**Table A1.** The updated nitrogen volume reactions considered in the N<sub>2</sub> model compared to our previous work [32], see notes below the table. The reaction number in this work corresponds to that in [32]. ‘N<sub>2</sub>’ in this table represents N<sub>2</sub>(v = 0). The rate coefficient units are given in s<sup>-1</sup>, m<sup>3</sup> s<sup>-1</sup> and m<sup>6</sup> s<sup>-1</sup> for one-, two- and three-body reactions, respectively. T<sub>e</sub> is in eV and T<sub>g</sub> in K, if not stated otherwise. The rate coefficient for cases marked with f(ε) is taken from a look-up-table calculated via the referred cross-section self-consistently coupled to the EEDF [58]. The reverse reaction rate coefficients of the electron-impact excitation labeled with a symbol ‘\*’ near the number are calculated via the principle of *detailed balancing* [67].

# <sup>b-d</sup>	Reaction	Rate coefficient	References
1*	$e + N(^4S) \rightarrow e + N(^2D)$	$f(\epsilon)$	[72]
2	$e + N(^4S) \rightarrow 2e + N^+$	$f(\epsilon)$	[72]
3 <sup>m</sup>	$e + N(^2D) \rightarrow 2e + N^+$	$f(\epsilon)$	[72]
4	$e + N_2 \rightarrow e + N(^4S) + N(^4S)$	$f(\sigma)$	[76] <sup>a</sup>
5	$e + N_2 \rightarrow e + N(^4S) + N(^2D)$	$f(\sigma)$	[76] <sup>a</sup>
6*	$e + N_2 \rightarrow e + N_2(A^3\Sigma)$	$f(\epsilon)$	[72]
7*	$e + N_2 \rightarrow e + N_2(B^3\Pi)$	$f(\epsilon)$	[72]
8	$e + N_2 \rightarrow 2e + N_2^+$	$f(\epsilon)$	[72]
9 <sup>i</sup>	$e + N_2 \rightarrow 2e + N^+ + N(^2D)$	$5.88 \times 10^{-16} T_e^{1.17} \exp(-22.36/T_e)$	[93, 94]
10 <sup>i</sup>	$e + N_2 \rightarrow 3e + N^+ + N^+$	$9.95 \times 10^{-16} T_e^{0.56} \exp(-43.62/T_e)$	[93, 94]
11 <sup>i</sup>	$e + N_2(A^3\Sigma) \rightarrow 2e + N_2^+$	$1.08 \times 10^{-14} T_e^{0.71} \exp(-12.04/T_e)$	[93, 94]
12	$e + N_2(B^3\Pi) \rightarrow 2e + N_2^+$	$1.08 \times 10^{-14} T_e^{0.71} \exp(-12.04/T_e)$	[93]
13 <sup>m</sup>	$2e + N^+ \rightarrow e + N(^4S)$	$1 \times 10^{-31} (300/T_e[K])^{4.5}$	[95]
14 <sup>i</sup>	$e + N^+ + N_2 \rightarrow N(^4S) + N_2$	$6 \times 10^{-39} (300/T_e[K])^{1.5}$	[95–97]
15 <sup>i</sup>	$e + N^+ + N(^4S) \rightarrow N(^4S) + N(^4S)$	$6 \times 10^{-39} (300/T_e[K])^{1.5}$	[96, 97]
17 <sup>m</sup>	$e + N_2^+ \rightarrow 2N(^4S)$	$2.8 \times 10^{-13} (300/T_e[K])^{0.5}$	[95]
18 <sup>m</sup>	$e + N_2^+ \rightarrow N(^2D) + N(^4S)$	$2 \times 10^{-13} (300/T_e[K])^{0.5}$	[95]
20 <sup>m</sup>	$2e + N_2^+ \rightarrow e + N_2$	$1 \times 10^{-31} (300/T_e[K])^{4.5}$	[95]
21 <sup>i</sup>	$e + N_3^+ \rightarrow N(^4S) + N_2$	$2 \times 10^{-13} (300/T_e[K])^{0.5}$	[96, 97]
22 <sup>m</sup>	$e + N_4^+ \rightarrow 2N_2$	$2 \times 10^{-12} (300/T_e[K])^{0.5}$	[95]
23 <sup>m</sup>	$2e + N_4^+ \rightarrow e + 2N_2$	$1 \times 10^{-31} (300/T_e[K])^{4.5}$	[95]
33 <sup>i</sup>	$N^+ + N(^4S) + N(^4S) \rightarrow N_2^+ + N(^4S)$	$3.3 \times 10^{-43} (300/T_g)^{0.75}$	[96, 97]
35 <sup>i</sup>	$N^+ + N(^4S) + N_2 \rightarrow N_2^+ + N_2$	$1 \times 10^{-41}$	[95–97]
36 <sup>i</sup>	$N^+ + N_2 \rightarrow N(^4S) + N_2^+$	$4.45 \times 10^{-16}$	[96, 97]
38 <sup>m</sup>	$N_2^+ + N(^4S) \rightarrow N_2 + N^+$	$2.4 \times 10^{-21} T_g$	[95]
39 <sup>i</sup>	$N_2^+ + N(^4S) + N_2 \rightarrow N_3^+ + N_2$	$9 \times 10^{-42} \exp(400/T_g)$	[95–97]
41 <sup>i</sup>	$N_2^+ + N(^2D) \rightarrow N_2 + N^+$	$1 \times 10^{-16}$	[98]
43 <sup>i</sup>	$N_2^+ + 2N_2 \rightarrow N_4^+ + N_2$	$5 \times 10^{-41}$	[95, 99]
44	$N_2^+ + N_2(A^3\Sigma) \rightarrow N_3^+ + N(^4S)$	$3 \times 10^{-16}$	[95]
45 <sup>i</sup>	$N_3^+ + N(^4S) \rightarrow N_2^+ + N_2$	$6.6 \times 10^{-17}$	[95–97]
46 <sup>i</sup>	$N_3^+ + N_2 \rightarrow N_2^+ + N(^4S) + N_2$	$6.6 \times 10^{-17}$	[96, 97]
47 <sup>i</sup>	$N_4^+ + N(^4S) \rightarrow 2N_2 + N^+$	$1 \times 10^{-17}$	[95]
48 <sup>m</sup>	$N_4^+ + N_2 \rightarrow 2N_2 + N_2^+$	$2.1 \times 10^{-22} \exp(T_g/121)$	[83](P.179)
54	$N(^4S) + N(^4S) + N(^4S) \rightarrow N(^4S) + N_2(A^3\Sigma)$	$1 \times 10^{-44}$	[100]
55	$N(^4S) + N(^4S) + N_2 \rightarrow N_2 + N_2$	$8.27 \times 10^{-46} \exp(500/T_g)$	[95]
56	$N(^4S) + N(^4S) + N_2 \rightarrow N_2 + N_2(A^3\Sigma)$	$8.27 \times 10^{-46} \exp(500/T_g)$	[95]
57 <sup>i</sup>	$N(^4S) + N(^4S) + N_2 \rightarrow N_2 + N_2(B^3\Pi)$	$8.27 \times 10^{-46} \exp(500/T_g)$	[95, 101]
59 <sup>i+</sup>	$N(^4S) + N_2(A^3\Sigma) \rightarrow N_2 + N(^2D)$	$4 \times 10^{-17}$	[97, 102]
62 <sup>m</sup>	$N_2 + N(^2D) \rightarrow N(^4S) + N_2$	$6 \times 10^{-21}$	[95]
63 <sup>m</sup>	$N_2 + N_2(A^3\Sigma) \rightarrow N_2 + N_2$	$3.0 \times 10^{-24}$	[95, 103, 104]
64 <sup>m</sup>	$N_2 + N_2(B^3\Pi) \rightarrow N_2 + N_2$	$1.5 \times 10^{-18}$	[105–107]

(Continued.)

**Table A1.** (Continued.)

65 <sup>††</sup>	$N_2 + N_2(B^3\Pi) \rightarrow N_2(A^3\Sigma) + N_2$	$5 \times 10^{-17}$	[95]
67 <sup>†</sup>	$2N_2(A^3\Sigma) \rightarrow N_2(B^3\Pi) + N_2$	$7.7 \times 10^{-17}$	[96, 97, 108]
70 <sup>†</sup>	$N_2(B^3\Pi) \rightarrow N_2(A^3\Sigma)$	$2 \times 10^5$	[96, 97, 109]

<sup>†</sup> Compared to our previous work [32], the ‘Ref’ is updated.

<sup>††</sup> Compared to our previous work [32], the ‘Rate coefficient’ and the ‘Ref’ are updated. In particular, the update for those of reactions 17, 18 and 48 is important for a better description of the electron density decay rate during the power decay of the power-on phase depicted in figure 4(a) and a better description of the ratio of  $N_4^+$  density to  $N_2^+$  density (not shown in this study).

<sup>†+</sup> Compared to our previous work [32], the ‘Reaction’ and the ‘Ref’ are updated.

<sup>a</sup> The rate coefficient for cases marked with  $f(\sigma)$  is directly evaluated according to the calculated EEDF and the corresponding electron-impact cross-section from ‘Ref’.

<sup>b</sup> The ‘Reaction’ containing helium species in [32] (i.e. reactions 16, 24-32, 34, 37, 40, 42, 49-53 and 58) are removed.

<sup>c</sup> The ‘Reaction’ in [32] (i.e. reactions 19, 60 and 61) are removed due to their negligible influence on the simulation results in this work.

<sup>d</sup> The ‘Reaction’ in [32] (i.e. reactions 66, 68, 69, 71 and 72) are removed due to an improved treatment of the chemical kinetics of electronically excited nitrogen molecules.

**Table A2.** The updated nitrogen vibrational kinetics considered in the  $N_2$  model compared to our previous work [32], see notes below the table. The reaction number in this work corresponds to that in [32]. The letters  $v$  and  $w$  represent the vibrationally excited levels of the nitrogen molecule. The rate coefficient for cases marked with  $f(\epsilon)$  is taken from a look-up-table calculated via the referred cross-section. Only the cross-sections of the first six vibrational levels are used in the solution to the Boltzmann equation [58], while those of the higher levels are directly evaluated to the rate coefficients according to the calculated EEDF and the corresponding electron-impact cross-section from ‘Ref’. The reverse reaction rate coefficient of the electron-impact excitation labeled with a symbol ‘\*’ near the number is calculated via the principle of *detailed balancing* [67]. The reverse reaction rate coefficients of the V-V and V-T mechanism labeled with a symbol ‘+’ near the number are calculated by equations (28) and (29), respectively.

# <sup>c</sup>	Reaction	Rate coefficient	References
1*	$e + N_2(v \geq 0) \rightarrow e + N_2(v < w)$	$f(\epsilon)$	[75, 76]
2	$e + N_2(v > 0) \rightarrow e + N(^4S) + N(^4S)$	$f(\sigma)$	[75, 76] <sup>a</sup>
3	$e + N_2(v = 1 - 35) \rightarrow e + N(^4S) + N(^2D)$	$f(\sigma)$	[76] <sup>a</sup>
4	$e + N_2(v = 1 - 40) \rightarrow e + e + N_2^+$	$f(\sigma)$	[76] <sup>a</sup>
5 <sup>+</sup>	$N_2(v) + N(^4S) \rightarrow N_2(w) + N(^4S)$ , ( $v > w$ )	see section 4.2	<sup>b</sup>
6 <sup>+</sup>	$N_2(v) + N_2(v = 0) \rightarrow N_2(v - 1) + N_2(v = 0)$	see section 4.2	<sup>b</sup>
8 <sup>+</sup>	$N_2(v) + N_2(w - 1) \rightarrow N_2(v - 1) + N_2(w)$ , ( $v \leq w - 1$ )	see section 4.1	<sup>b</sup>

<sup>a</sup> The rate coefficient for cases marked with  $f(\sigma)$  is directly evaluated in accordance with the calculated EEDF and the corresponding electron-impact cross-section from ‘Ref’.

<sup>b</sup> Compared to our previous work [32], the ‘Reaction’, ‘Rate Coefficient’ and ‘Ref’ of the reactions 5, 6 and 8 are updated. Several distinct methods among the literature are used to approximate the V-V and V-T rate coefficients, see sections 4.1 and 4.2, respectively.

<sup>c</sup> The ‘Reaction’ containing helium species in [32] (i.e. reactions 7, 9, 10 and 11) are removed.

**Table A3.** The additionally considered nitrogen volume reactions in the  $N_2$  model compared to our previous work [32]. ‘ $N_2$ ’ in this table represents  $N_2(v=0)$ . The rate coefficient units are given in  $s^{-1}$  and  $m^3 s^{-1}$  for one- and two-body reactions, respectively.  $T_g$  is in K. The rate coefficient for cases marked with  $f(\epsilon)$  is taken from a look-up-table calculated via the referred cross-section self-consistently coupled to the EEDF [58]. The reverse reaction rate coefficients of the electron-impact excitation labeled with a symbol ‘\*’ near the number are calculated via the principle of *detailed balancing* [67]. For the ‘Reaction’ labeled with a symbol ‘~’ near the number, the ‘Rate coefficient’ is estimated in the ‘Ref’.

#	Reaction	Rate Coefficient	References
1*	$e + N(^4S) \rightarrow e + N(^2P)$	$f(\epsilon)$	[72]
2*	$e + N(^2D) \rightarrow e + N(^2P)$	$f(\epsilon)$	[72]
3	$e + N(^2P) \rightarrow e + e + N^+$	$f(\epsilon)$	[72]
4	$e + N_2 \rightarrow e + N_2(W^3\Delta)$	$f(\epsilon)$	[72]
5	$e + N_2 \rightarrow e + N_2(B'^3\Sigma)$	$f(\epsilon)$	[72]
6	$e + N_2 \rightarrow e + N_2(a'^1\Sigma)$	$f(\epsilon)$	[72]
7	$e + N_2 \rightarrow e + N_2(a^1\Pi)$	$f(\epsilon)$	[72]
8	$e + N_2 \rightarrow e + N_2(w^1\Delta)$	$f(\epsilon)$	[72]
9	$e + N_2 \rightarrow e + N_2(C^3\Pi)$	$f(\epsilon)$	[72]
10	$e + N_2 \rightarrow e + N_2(E^3\Sigma)$	$f(\epsilon)$	[72] <sup>a</sup>
11	$e + N_2 \rightarrow e + N_2(a'^1\Sigma)$	$f(\epsilon)$	[72] <sup>a</sup>
12	$e + N_2 \rightarrow e + N_2(\text{singlets}^*)$	$f(\epsilon)$	[72] <sup>a</sup>
13	$e + N_2 \rightarrow e + e + N_2^+(B)$	$f(\epsilon)$	[72]
14	$N_2^+(B) \rightarrow N_2^+$	$1.61 \times 10^7$	[110]
15	$N_2^+(B) + N_2 \rightarrow N_2^+ + N_2$	$2.1 \times 10^{-16}$	[110]
16	$N(^2D) + N(^2P) \rightarrow e + N_2^+$	$1.92 \times 10^{-21} T_g^{0.98} / (1 - \exp(-3129/T_g))$	[73, 111]
17	$N(^2P) + N(^2P) \rightarrow e + N_2^+$	$3.2 \times 10^{-21} T_g^{0.98} / (1 - \exp(-3129/T_g))$	[73, 111]
18	$N(^2P) + N_2(a'^1\Sigma) \rightarrow e + N_3^+$	$1.0 \times 10^{-17}$	[73, 111]
19~	$N_2(A^3\Sigma) + N_2(a'^1\Sigma) \rightarrow e + N_4^+$	$3.2 \times 10^{-18}$	[73, 100] <sup>b</sup>
20~	$N_2(a'^1\Sigma) + N_2(a'^1\Sigma) \rightarrow e + N_4^+$	$1.0 \times 10^{-17}$	[73, 112] <sup>b</sup>
21	$N(^2P) + N(^4S) \rightarrow N(^2D) + N(^4S)$	$1.8 \times 10^{-18}$	[73, 95, 111]
22	$N(^2P) + N_2 \rightarrow N(^2D) + N_2$	$2.0 \times 10^{-24}$	[95]
23	$N(^2P) + N_2 \rightarrow N(^4S) + N_2$	$3.0 \times 10^{-23}$	[38, 113]
24	$N_2(A^3\Sigma) + N(^4S) \rightarrow N(^2P) + N_2$	$4.0 \times 10^{-17}$	[73, 102, 114]
25	$N_2(A^3\Sigma) + N_2(A^3\Sigma) \rightarrow N_2(C^3\Pi) + N_2$	$1.5 \times 10^{-16}$	[73, 115]
26	$N_2(B^3\Pi) + N_2 \rightarrow N_2(W^3\Delta) + N_2$	$7.0 \times 10^{-18}$	[73, 116]
27~	$N_2(W^3\Delta) + N_2 \rightarrow N_2 + N_2$	$3.0 \times 10^{-17}$	[73, 108, 117]
28	$N_2(W^3\Delta) + N_2 \rightarrow N_2(B^3\Pi) + N_2$	$1.2 \times 10^{-16}$	[73, 118]
29	$N_2(a'^1\Sigma) + N_2 \rightarrow N_2(B^3\Pi) + N_2$	$1.9 \times 10^{-19}$	[73, 95, 119]
30~	$N_2(a'^1\Sigma) + N_2 \rightarrow N_2(a^1\Pi) + N_2$	$1.82 \times 10^{-17} \exp(-1700/T_g)$	[73, 100]
31	$N_2(a^1\Pi) \rightarrow N_2(a'^1\Sigma)$	$1.91 \times 10^2$	[73, 77, 120]
32	$N_2(a^1\Pi) \rightarrow N_2$	$1.8 \times 10^4$	[73, 77, 121]
33	$N_2(a^1\Pi) + N_2 \rightarrow N_2(a'^1\Sigma) + N_2$	$2 \times 10^{-17}$	[77, 121]
34~	$N_2(w^1\Delta) + N_2 \rightarrow N_2 + N_2$	$3.0 \times 10^{-17}$	[73, 108, 117]
35	$N_2(C^3\Pi) \rightarrow N_2(B^3\Pi)$	$2.74 \times 10^7$	[73, 77, 122]
36	$N_2(C^3\Pi) + N_2 \rightarrow 2N_2$	$0.09 \times 10^{-16}$	[110]
37	$N_2(a'^1\Sigma) + N_2 \rightarrow N_2 + N_2$	$2.3 \times 10^{-16}$	[73, 123] <sup>a</sup>

<sup>a</sup> Only a limited number of the reaction channels of  $N_2(E^3\Sigma)$ ,  $N_2(a'^1\Sigma)$ ,  $N_2(\text{singlets}^*)$  is available in the literature. The calculated densities of these electronically excited states of nitrogen molecule are potentially unrealistic. However, the inclusion of these states does not affect the present results, as discussed in appendix C, where the ‘Reaction’ containing these states (i.e. reactions 10-12 and 37) are removed from the chemical set in an additional simulation for a sensitivity analysis.

<sup>b</sup> The rate coefficients of reactions 19 and 20 were estimated in [73, 100, 112]. These estimated values used in the reference chemical set of appendix A are replaced with the rate coefficient values used in [77, 105], which gave the best agreement between the measurement data and simulation results in [105], in an additional simulation presented and discussed in appendix C.

**Table A4.** The neutral wall reactions included in the N<sub>2</sub> model. The updates compared to our previous work [32] see notes below the table. The reaction number in this work corresponds to that in [32]. ‘N<sub>2</sub>’ in this table represents N<sub>2</sub>(v = 0).

# <sup>d</sup>	Reaction	Probability(γ)	References
3	N( <sup>2</sup> D) + wall → N( <sup>4</sup> S)	0.93	[70]
4	N <sub>2</sub> (A <sup>3</sup> Σ) + wall → N <sub>2</sub>	1	[70]
5	N <sub>2</sub> (B <sup>3</sup> Π) + wall → N <sub>2</sub>	1	[70]
6	N( <sup>4</sup> S, <sup>2</sup> D) + wall → 1/2N <sub>2</sub>	10 <sup>-6</sup>	[124]
11	N <sub>2</sub> (v) + wall → N <sub>2</sub> (v - 1)	3 × 10 <sup>-3</sup>	[74] <sup>a</sup>
-----			
Reactions related to the additionally considered species in this work compared to [32]:			
14	N( <sup>2</sup> P) + wall → N( <sup>4</sup> S)	0.93	<i>b</i>
15	N <sub>2</sub> (W <sup>3</sup> Δ) + wall → N <sub>2</sub>	1	<i>b</i>
16	N <sub>2</sub> (B' <sup>3</sup> Σ) + wall → N <sub>2</sub>	1	<i>b</i>
17	N <sub>2</sub> (a' <sup>1</sup> Σ) + wall → N <sub>2</sub>	1	<i>b</i>
18	N <sub>2</sub> (a <sup>1</sup> Π) + wall → N <sub>2</sub>	1	<i>b</i>
19	N <sub>2</sub> (w <sup>1</sup> Δ) + wall → N <sub>2</sub>	1	<i>b</i>
20	N <sub>2</sub> (C <sup>3</sup> Π) + wall → N <sub>2</sub>	1	<i>b</i>
21	N <sub>2</sub> (E <sup>3</sup> Σ) + wall → N <sub>2</sub>	1	<i>b, c</i>
22	N <sub>2</sub> (a'' <sup>1</sup> Σ) + wall → N <sub>2</sub>	1	<i>b, c</i>
23	N <sub>2</sub> (singlets*) + wall → N <sub>2</sub>	1	<i>b, c</i>
24	N( <sup>2</sup> P) + wall → 1/2N <sub>2</sub>	10 <sup>-6</sup>	<i>b</i>

<sup>a</sup> The wall reaction probability  $\gamma = 1$  of N<sub>2</sub>(v) + wall → N<sub>2</sub>(v - 1) used in [32] (referring to a simulation study [70]) is updated in this work with  $\gamma = 3 \times 10^{-3}$  (based on an experimental work [74] which gives a range of  $4 \times 10^{-4}$  to  $3 \times 10^{-3}$  for the wall deactivation probabilities of N<sub>2</sub>(v = 1) under different surface materials and operating conditions).  $\gamma = 3 \times 10^{-3}$ , as the maximal value, is chosen for the deactivation probabilities of N<sub>2</sub>(0 < v < 58).

<sup>b</sup> The neutral wall reaction probabilities of the additionally considered higher electronically excited states are assumed to be identical to those of the lower ones.

<sup>c</sup> Only a limited number of the reaction channels of N<sub>2</sub>(E<sup>3</sup>Σ), N<sub>2</sub>(a''<sup>1</sup>Σ), N<sub>2</sub>(singlets\*) is available in the literature. The calculated densities of these electronically excited states of nitrogen molecule are potentially unrealistic. However, the inclusion of these states does not affect the present results, as discussed in appendix C, where the ‘Reaction’ containing these states (i.e. reactions 21–23) are removed from the chemical set in an additional simulation for a sensitivity analysis.

<sup>d</sup> The ‘Reaction’ containing helium or oxygen species in [32] (i.e. reactions 1–2, 7–10 and 12–13) are removed.

**Table A5.** The stepwise dissociation mechanism in the N<sub>2</sub> model by a vibrational quantum at the pseudo level v' = 58. The reaction number in this work corresponds to that in [32]. The letters v and w represent the vibrational quantum numbers. ‘N<sub>2</sub>’ in this table represents N<sub>2</sub>(v = 0).

# <sup>b</sup>	Reaction	References
SD-1	$e + N_2(v \geq 0) \rightarrow N_2(v') + e \rightarrow 2N(^4S) + e$	<i>a</i>
SD-2	$N(^4S) + N_2(w) \rightarrow N(^4S) + N_2(v') \rightarrow 3N(^4S), v' - w = 1 - 5$	<i>a</i>
SD-3	$N_2 + N_2(v' - 1) \rightarrow N_2 + N_2(v') \rightarrow N_2 + 2N(^4S)$	<i>a</i>
SD-5	$N_2(v' - 1) + N_2(w > 0) \rightarrow N_2(v') + N_2(w - 1) \rightarrow 2N(^4S) + N_2(w - 1)$	<i>a</i>

<sup>a</sup> The rate coefficients of these reactions are identical to those of the corresponding reactions in table A2.

<sup>b</sup> The ‘Reaction’ containing helium species in [32] (i.e. reaction SD-4) is removed.

**Table A6.** The electron-impact elastic collisions in the model of N<sub>2</sub>. The reaction number in this work corresponds to that in [32]. ‘N<sub>2</sub>’ in this table represents N<sub>2</sub>(v = 0).

# <sup>a</sup>	Collision	References
2 <sup>1</sup>	$e + N(^4S) \rightarrow e + N(^4S)$	[72]
3 <sup>1</sup>	$e + N_2 \rightarrow e + N_2$	[72]

<sup>1</sup> Compared to our previous work [32], the ‘Ref’ is updated.

<sup>a</sup> The ‘Reaction’ containing helium or oxygen species in [32] (i.e. reactions 1 and 4–9) are removed.

## Appendix B. Variation of power-on duration and peak power value

The validation of the electron density and the ratios of the  $N_2(v = 1, 2, 3, 4)$  densities to the gas density is conducted with a variation of the power-on duration & peak power value. The parameters used in this study are (a) 200 ns & 17 kW see figure 4, (b) 250 ns & 17 kW and (c) 200 ns & 29 kW see figures B1 and B2, respectively. For the sake of simplicity, the power set (a) 200 ns and 17 kW is considered in all the simulation results in section 5, whereas the sets (b) and (c) are merely used in appendix B. The outcomes of figures B1 and B2 in appendix B are similar to those of figure 4 in section 5.1.

## Appendix C. Additional simulations considering two different chemical sets compared to those in appendix A

Additional simulations considering two different chemical sets compared to those in appendix A are conducted for a sensitivity analysis. For the sake of simplicity, these additional simulation results considering the ‘ChemSet 1’ or the ‘ChemSet 2’ (explained below) are only compared to the ‘Sim. (SSH)’ results presented in figure 4 (using the reference chemical set in appendix A).

The first chemical set ‘ChemSet 1’ is that the electronically excited states of nitrogen molecule  $N_2(E^3\Sigma)$ ,  $N_2(a'^1\Sigma)$ ,  $N_2(\text{singlets}^*)$  are removed from the reference chemical set in appendix A due to the limited number of their reaction channels available in the literature and the possibility of  $N_2(\text{singlets}^*)$  accounting for some pre-dissociative states, which result in potentially unrealistic species density calculations. Specifically, reactions 10–12 and 37 in table A3 and reactions 21–23 in table A4 are excluded in the particle

balance equation (see equation (2)), and only the electron energy loss of reactions 10–12 in table A3 is considered in the electron energy balance equation (see equation (7)). The same electron density and ratios of the  $N_2(v = 1, 2, 3, 4)$  densities to the gas density are obtained between the simulation results using the reference chemical set in appendix A and using the ‘ChemSet 1’ in appendix C, see figure C1. The same  $N_2(v = 0)$  density within one pulse period is acquired between these two cases (not shown here). The simulation results investigated in this work are not sensitive to the reaction channels of  $N_2(E^3\Sigma)$ ,  $N_2(a'^1\Sigma)$ ,  $N_2(\text{singlets}^*)$  considered in the reference chemical set in appendix A.

The second chemical set ‘ChemSet 2’ is that the rate coefficients of reactions 19 and 20 in table A3 from the reference chemical set in appendix A are replaced with the rate coefficient values used in [77, 105], which gave the best agreement between the measurement data and simulation results in [105]. Specifically, the estimated value  $3.2 \times 10^{-18} \text{ m}^3 \text{ s}^{-1}$  [73, 100] of reaction 19:  $N_2(A^3\Sigma) + N_2(a'^1\Sigma) \rightarrow e + N_4^+$  is replaced with the experimentally-defined value  $1.0 \times 10^{-17} \text{ m}^3 \text{ s}^{-1}$  [77, 105], and the estimated value  $1.0 \times 10^{-17} \text{ m}^3 \text{ s}^{-1}$  [73, 112] of reaction 20:  $N_2(a'^1\Sigma) + N_2(a'^1\Sigma) \rightarrow e + N_4^+$  is replaced with the experimentally-defined value  $5.0 \times 10^{-17} \text{ m}^3 \text{ s}^{-1}$  [77, 105]. The same ratios of the  $N_2(v = 1, 2, 3, 4)$  densities to the gas density are obtained between the simulation results using the reference chemical set in appendix A and using the ‘ChemSet 2’ in appendix C, see figure C2. However, it is predicted that the electron density in the early afterglow calculated with the reference chemical set is a little bit smaller than that calculated with the ‘ChemSet 2’, e.g. the former is smaller than the latter around by a factor of 1.28 at 400 ns. This is ascribed to the following two points: (i) reactions 19 and 20 in table A3 play a role in the electron production during the early afterglow, and (ii) the rate coefficients of reactions 19 and 20 from the reference chemical set are smaller than those from the ‘ChemSet 2’.

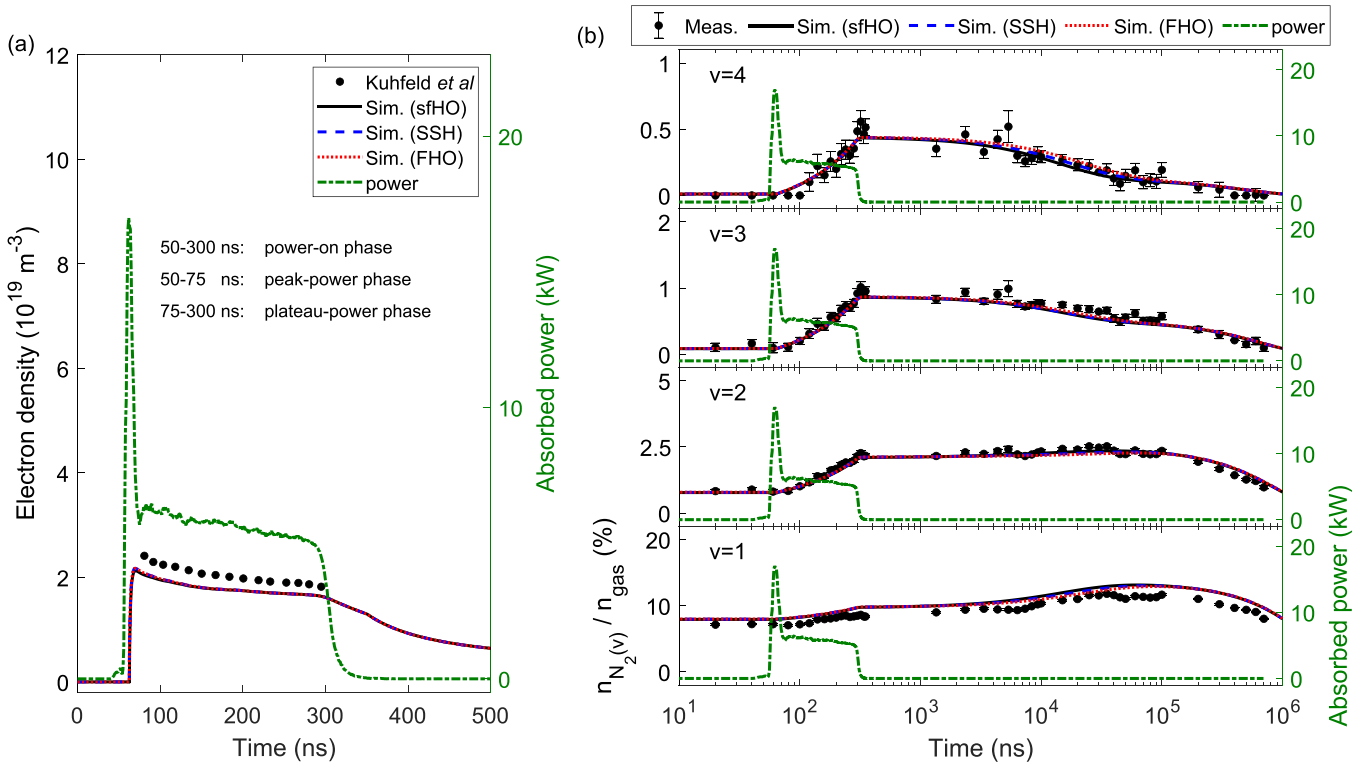


Figure B1. As in figure 4, but for 250 ns power-on duration.

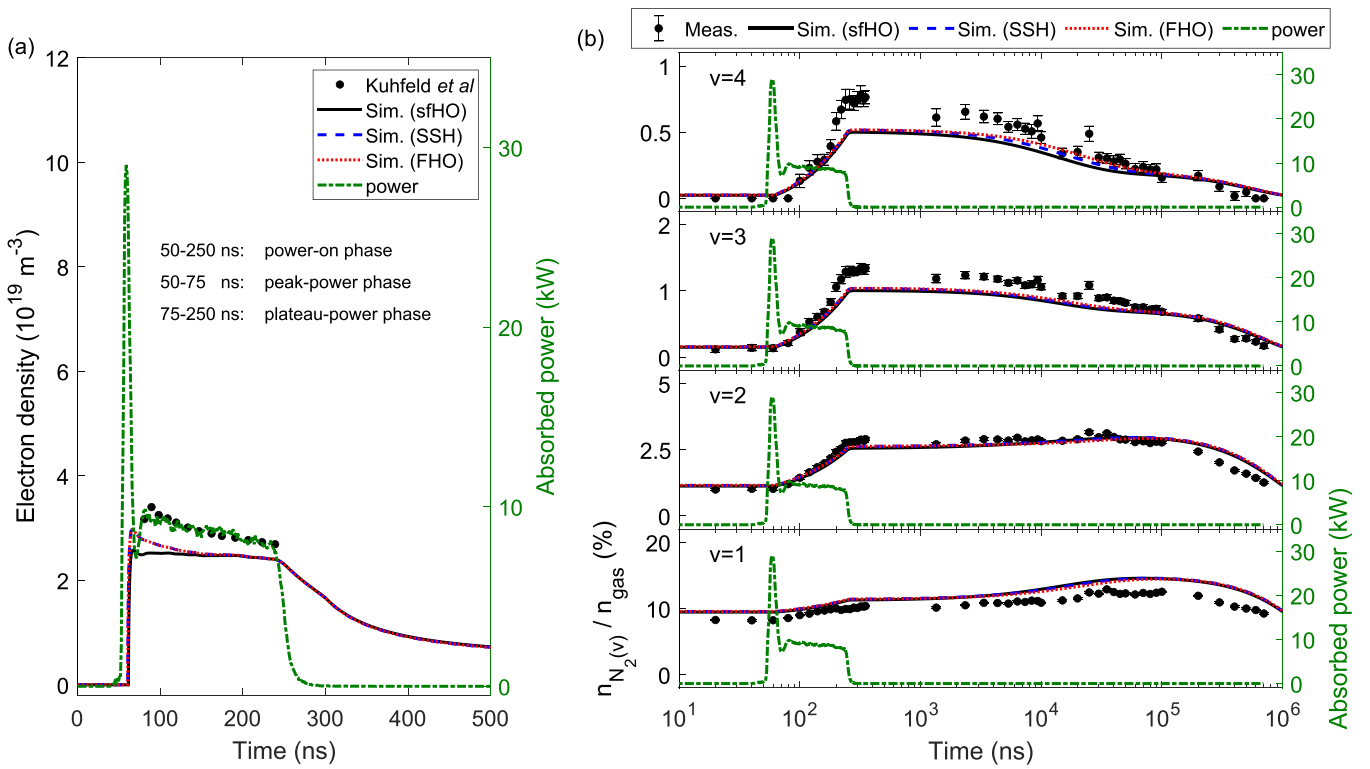
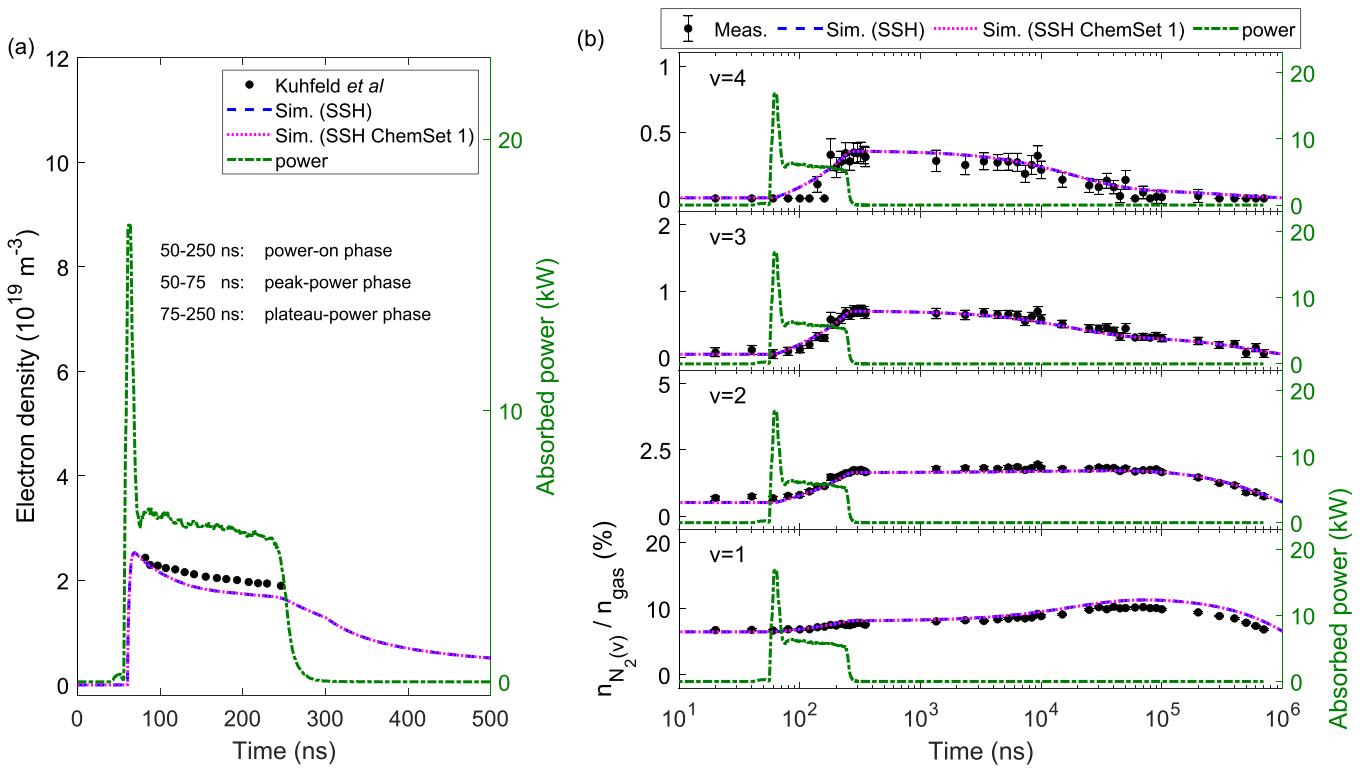
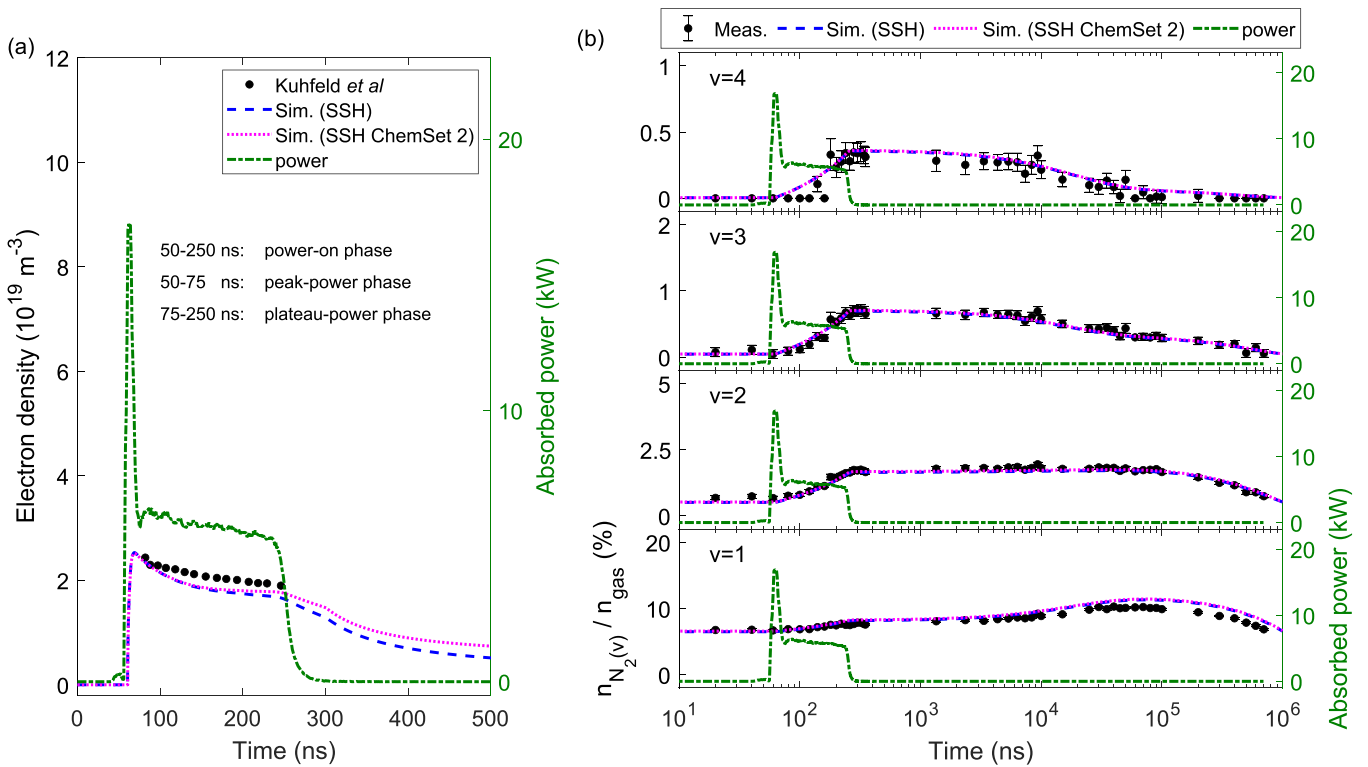


Figure B2. As in figure 4, but for 29 kW peak power value.



**Figure C1.** As in figure 4, but the  $\text{N}_2\text{-N}_2$  V-V rate coefficient scaling law is only calculated with the SSH approach. The electron density and the density ratios are calculated by the 0-D model using the reference chemical set provided in appendix A (---) and using the chemical set ‘ChemSet 1’ explained in appendix C (.....).



**Figure C2.** As in figure 4, but the  $\text{N}_2\text{-N}_2$  V-V rate coefficient scaling law is only calculated with the SSH approach. The electron density and the density ratios are calculated by the 0-D model using the reference chemical set provided in appendix A (---) and using the chemical set ‘ChemSet 2’ explained in appendix C (.....).

## ORCID iDs

Youfan He  <https://orcid.org/0000-0003-1275-7695>  
 Jan Kuhfeld  <https://orcid.org/0000-0003-2335-2634>  
 Nikita D Lepikhin  <https://orcid.org/0000-0002-4027-5792>  
 Uwe Czarnetzki  <https://orcid.org/0000-0002-5823-1501>  
 Vasco Guerra  <https://orcid.org/0000-0002-6878-6850>  
 Ralf Peter Brinkmann  <https://orcid.org/0000-0002-2581-9894>  
 Andrew R Gibson  <https://orcid.org/0000-0002-1082-4359>  
 Efe Kemaneci  <https://orcid.org/0000-0002-5540-0947>

## References

- [1] Graves D B 2012 The emerging role of reactive oxygen and nitrogen species in redox biology and some implications for plasma applications to medicine and biology *J. Phys. D: Appl. Phys.* **45** 263001
- [2] Sun Ja Kim T H C, Bae S H and Leem S H 2010 Induction of apoptosis in human breast cancer cells by a pulsed atmospheric pressure plasma jet *Appl. Phys. Lett.* **97** 023702
- [3] Yeong Kim D, Kim S J, Min Joh H and Chung T H 2018 Characterization of an atmospheric pressure plasma jet array and its application to cancer cell treatment using plasma activated medium *Phys. Plasmas* **25** 073505
- [4] Athanasopoulos D, Svarnas P, Ladas S Kennou S and Koutsoukos P 2018 On the wetting properties of human stratum corneum epidermidis surface exposed to cold atmospheric-pressure pulsed plasma *Appl. Phys. Lett.* **112** 213703
- [5] Shao T, Wang R, Zhang C and Yan P 2018 Atmospheric-pressure pulsed discharges and plasmas: mechanism, characteristics and applications *High Volt.* **3** 14–20
- [6] Taghvaei H, Jahanmiri A, Reza Rahimpour M, Mohamadzadeh Shirazi M and Hooshmand N 2013 Hydrogen production through plasma cracking of hydrocarbons: Effect of carrier gas and hydrocarbon type *Chem. Eng. J.* **226** 384–92
- [7] Zhu B, Liu J-L, Xiao-Song Li, Liu J-B, Zhu X and Zhu A-M 2017 In situ regeneration of au nanocatalysts by atmospheric-pressure air plasma: regeneration characteristics of square-wave pulsed plasma *Top. Catal.* **60** 914–24
- [8] Bogaerts A and Erik C N 2018 Plasma technology: An emerging technology for energy storage *ACS Energy Lett.* **3** 1013–27
- [9] Chen J G et al 2018 Beyond fossil fuel-driven nitrogen transformations *Science* **360** eaar6611
- [10] Mehta P, Barboun P, Herrera F A, Kim J, Rumbach P, David B G, Hicks J C and Schneider W F 2018 Overcoming ammonia synthesis scaling relations with plasma-enabled catalysis *Nat. Catal.* **1** 269–75
- [11] Barboun P, Mehta P, Herrera F A, David B G, Schneider W F and Hicks J C 2019 Distinguishing plasma contributions to catalyst performance in plasma-assisted ammonia synthesis *ACS Sustain. Chem. Eng.* **7** 8621–30
- [12] Peng P, Yun Li, Cheng Y, Deng S, Chen P and Ruan R 2016 Atmospheric pressure ammonia synthesis using non-thermal plasma assisted catalysis *Plasma Chem. Plasma Process.* **36** 1201–10
- [13] Iwasaki M, Matsudaira Y, Takeda K, Ito M, Miyamoto E, Yara T, Uehara T and Hori M 2008 Roles of oxidizing species in a nonequilibrium atmospheric-pressure pulsed remote O<sub>2</sub>/N<sub>2</sub> plasma glass cleaning process *J. Appl. Phys.* **103** 023303
- [14] Chiang M-H, Liao K-C, Lin I-M, Lu C-C, Huang H-Y, Kuo C-L, Wu J-S, Hsu C-C and Chen S-H 2010 Effects of oxygen addition and treating distance on surface cleaning of ito glass by a non-equilibrium nitrogen atmospheric-pressure plasma jet *Plasma Chem. Plasma Process.* **30** 553–63
- [15] Dowling D P, O'Neill F T, Langlais S J and Law V J 2011 Influence of dc pulsed atmospheric pressure plasma jet processing conditions on polymer activation *Plasma Process. Polym.* **8** 718–27
- [16] Nagamatsu H, Ichiki R, Yasumatsu Y, Inoue T, Yoshida M, Akamine S and Kanazawa S 2013 Steel nitriding by atmospheric-pressure plasma jet using N<sub>2</sub>/H<sub>2</sub> mixture gas *Surf. Coat. Technol.* **225** 26–33
- [17] Yuji T, Akatsuka H, Mungkung N, Park B W and Sung Y M 2008 Surface treatment of TiO<sub>2</sub> films for dye-sensitized solar cells using atmospheric-pressure non-equilibrium DC pulse discharge plasma jet *Vacuum* **83** 124–7
- [18] Toshifuji J, Katsumata T, Takikawa H, Sakakibara T and Shimizu I 2003 Cold arc-plasma jet under atmospheric pressure for surface modification *Surf. Coat. Technol.* **171** 302–6
- [19] Tendo C, Tixier C, Tristant P, Desmaison J and Leprince P 2006 Atmospheric pressure plasmas: a review *Spectroch. Acta B* **61** 2–30
- [20] Winter J, Brandenburg R and Weltmann K-D 2015 Atmospheric pressure plasma jets: an overview of devices and new directions *Plasma Sources Sci. Technol.* **24** 064001
- [21] Viegas P, Slikboer E, Bonaventura Z, Guaitella O, Sobota A and Bourdon A 2022 Physics of plasma jets and interaction with surfaces: review on modelling and experiments *Plasma Sources Sci. Technol.* **31** 053001
- [22] Schutze A, Jeong J Y, Babayan S E, Park J, Selwyn G S and Hicks R F 1998 The atmospheric-pressure plasma jet: a review and comparison to other plasma sources *IEEE Trans. Plasma Sci.* **26** 1685–94
- [23] Lepikhin N D, Luggenhölscher D and Czarnetzki U 2020 Electric field measurements in a He:N<sub>2</sub> nanosecond pulsed discharge with sub-ns time resolution *J. Appl. Phys.* **54** 055201
- [24] Preissing P, Korolov I, Schulze J, von der Gathen V S and Böke M 2020 Three-dimensional density distributions of NO in the effluent of the cost reference microplasma jet operated in He/N<sub>2</sub>/O<sub>2</sub> *Plasma Sources Sci. Technol.* **29** 125001
- [25] Kuhfeld J, Lepikhin N D, Luggenhölscher D and Czarnetzki U 2021 Vibrational CARS measurements in a near-atmospheric pressure plasma jet in nitrogen. I. Measurement procedure and results *J. Appl. Phys.* **54** 305204
- [26] Stewig C, Schüttler S, Urbanietz T, Böke M and von Keudell A 2020 Excitation and dissociation of CO<sub>2</sub> heavily diluted in noble gas atmospheric pressure plasma *J. Phys. D: Appl. Phys.* **53** 125205
- [27] Murakami T, Niemi K, Gans T, O'Connell D and Graham W G 2012 Chemical kinetics and reactive species in atmospheric pressure helium-oxygen plasmas with humid-air impurities *Plasma Sources Sci. Technol.* **22** 015003
- [28] Schröter S et al 2018 Chemical kinetics in an atmospheric pressure helium plasma containing humidity *Phys. Chem. Chem. Phys.* **20** 24263–86
- [29] Kuhfeld J, Luggenhölscher D and Czarnetzki U 2021 Vibrational CARS measurements in a near-atmospheric pressure plasma jet in nitrogen: II. Analysis *J. Appl. Phys.* **54** 305205

- [30] Waskoenig J, Niemi K, Knake N, Graham L M, Reuter S, von der Gathen V S and Gans T 2010 Atomic oxygen formation in a radio-frequency driven micro-atmospheric pressure plasma jet *Plasma Sources Sci. Technol.* **19** 045018
- [31] Liu Y, Korolov I, Trieschmann J, Steuer D, von der Gathen V S, Böke M, Bischoff L, Hübner G, Schulze J and Mussenbrock T 2021 Micro atmospheric pressure plasma jets excited in He/O<sub>2</sub> by voltage waveform tailoring: a study based on a numerical hybrid model and experiments *Plasma Sources Sci. Technol.* **30** 064001
- [32] Youfan H et al 2021 Zero-dimensional and pseudo-one-dimensional models of atmospheric-pressure plasma jets in binary and ternary mixtures of oxygen and nitrogen with helium background *Plasma Sources Sci. Technol.* **30** 105017
- [33] Hayakawa R, Yoshimura T, Ashida A, Uehara T and Fujimura N 2006 Reaction of si with excited nitrogen species in pure nitrogen plasma near atmospheric pressure *Thin Solid Films* **506–507** 423–6
- [34] Ichiki R, Nagamatsu H, Yasumatsu Y, Iwao T, Akamine S and Kanazawa S 2012 Nitriding of steel surface by spraying pulsed-arc plasma jet under atmospheric pressure *Mater. Lett.* **71** 134–6
- [35] Carton O, Ben Salem D, Bhatt S, Pulpytel J and Arefi-Khonsari F 2012 Plasma polymerization of acrylic acid by atmospheric pressure nitrogen plasma jet for biomedical applications *Plasma Process. Polym.* **9** 984–93
- [36] Yang C-H, Kuok F-H, Liao C-Y, Wan T-H, Chen C-W, Cheng-Che Hsu I-C C and Chen J-Z 2017 Flexible reduced graphene oxide supercapacitor fabricated using a nitrogen dc-pulse atmospheric-pressure plasma jet *Mater. Res. Express* **4** 025504
- [37] Jui-Hsuan Tsai I-C C, Hsu C-C and Chen J-Z 2017 DC-pulse atmospheric-pressure plasma jet and dielectric barrier discharge surface treatments on fluorine-doped tin oxide for perovskite solar cell application *J. Phys. D: Appl. Phys.* **51** 025502
- [38] Davies H L, Guerra V, van der Woude M, Gans T, O'Connell D and Gibson A R 2023 Vibrational kinetics in repetitively pulsed atmospheric pressure nitrogen discharges: average-power-dependent switching behaviour *Plasma Sources Sci. Technol.* **32** 014003
- [39] Pai D Z, Stancu G D, Lacoste D A and Laux C O 2009 Nanosecond repetitively pulsed discharges in air at atmospheric pressure—the glow regime *Plasma Sources Sci. Technol.* **18** 045030
- [40] Norberg S A, Johnsen E and Kushner M J 2015 Formation of reactive oxygen and nitrogen species by repetitive negatively pulsed helium atmospheric pressure plasma jets propagating into humid air *Plasma Sources Sci. Technol.* **24** 035026
- [41] Kelly S and Turner M M 2014 Power modulation in an atmospheric pressure plasma jet *Plasma Sources Sci. Technol.* **23** 065012
- [42] Dedrick J, Schröter S, Niemi K, Wijaikhum A, Wagenaars E, de Oliveira N, Nahon L, Booth J P, O'Connell D and Gans T 2017 Controlled production of atomic oxygen and nitrogen in a pulsed radio-frequency atmospheric-pressure plasma *J. Phys. D: Appl. Phys.* **50** 455204
- [43] Teramoto Y, Ono R and Oda T 2012 Production mechanism of atomic nitrogen in atmospheric pressure pulsed corona discharge measured using two-photon absorption laser-induced fluorescence *J. Appl. Phys.* **111** 113302
- [44] Golda J et al 2016 Concepts and characteristics of the 'COST Reference Microplasma Jet *J. Phys. D: Appl. Phys.* **49** 084003
- [45] Lo A Cessou A, Boubert P and Vervisch P 2014 Space and time analysis of the nanosecond scale discharges in atmospheric pressure air: I. gas temperature and vibrational distribution function of N<sub>2</sub> and O<sub>2</sub> *J. Phys. D: Appl. Phys.* **47** 115201
- [46] Dedic C E, Meyer T R and Michael J B 2017 Single-shot ultrafast coherent anti-stokes raman scattering of vibrational/rotational nonequilibrium *Optica* **4** 563–70
- [47] Richards C, Jans E, Gulko I, Orr K and Adamovich I V 2022 N<sub>2</sub> vibrational excitation in atmospheric pressure ns pulse and RF plasma jets *Plasma Sources Sci. Technol.* **31** 034001
- [48] Vereshchagin K A, Smirnov V V and Shakhmatov V A 1997 Cars study of the vibrational kinetics of nitrogen molecules in the burning and afterglow stages of a pulsed discharge *Tech. Phys.* **42** 487–94
- [49] Montello A, Yin Z, Burnette D, Adamovich I V and Lempert W R 2013 Picosecond CARS measurements of nitrogen vibrational loading and rotational/translational temperature in non-equilibrium discharges *J. Phys. D: Appl. Phys.* **46** 464002
- [50] Shkurenkov I, Burnette D, Lempert W R and Adamovich I V 2014 Kinetics of excited states and radicals in a nanosecond pulse discharge and afterglow in nitrogen and air *Plasma Sources Sci. Technol.* **23** 065003
- [51] Yang W, Zhou Q and Dong Z 2016 Simulation study on nitrogen vibrational kinetics in a single nanosecond pulse high voltage air discharge *AIP Adv.* **6** 055209
- [52] Kuhfeld J, Lepikhin N D, Luggenhölscher D, Czarnetzki U and Donkó Z 2023 PIC/MCC simulation for a ns-pulsed glow discharge in nitrogen at sub-atmospheric pressure and analysis of its quasi-steady state physics *Plasma Sources Sci. Technol.* **32** 084001
- [53] Lepikhin N D, Kuhfeld J, Donkó Z, Luggenhölscher D and Czarnetzki U 2023 Breakdown and quasi-DC phase of a nanosecond discharge: Comparison of optical emission spectroscopy measurements with numerical simulations *Plasma Sources Sci. Technol.* **32** 084002
- [54] Rosa P, Karayiannis T G and Collins M W 2009 Single-phase heat transfer in microchannels: The importance of scaling effects *Appl. Therm. Eng.* **29** 3447–68
- [55] Liu D X, Bruggeman P, Iza F, Rong M Z and Kong M G 2010 Global model of low-temperature atmospheric-pressure He + H<sub>2</sub>O plasmas *Plasma Sources Sci. Technol.* **19** 025018
- [56] Turner M M 2015 Uncertainty and error in complex plasma chemistry models *Plasma Sources Sci. Technol.* **24** 035027
- [57] Schmidt-Bleker A, Winter J, Bösel A, Reuter S and Weltmann K-D 2015 On the plasma chemistry of a cold atmospheric argon plasma jet with shielding gas device *Plasma Sources Sci. Technol.* **25** 015005
- [58] Tejero del Caz A, Guerra V, Gonçalves D, Lino da Silva M, Marques L, Pinhao N, Pintassilgo C D and Alves L L 2019 The LisbOn KInetics boltzmann solver *Plasma Sources Sci. Technol.* **28** 043001
- [59] Capitelli M, Colonna G, Catella M, Capitelli F and Eletskaia A 2000 On the relaxation of electron energy distribution function in LIBS plasmas *Chem. Phys. Lett.* **316** 517–23
- [60] Tejero del Caz A, Guerra V, Pinhão N, Pintassilgo C D and Alves L L 2021 On the quasi-stationary approach to solve the electron boltzmann equation in pulsed plasmas *Plasma Sources Sci. Technol.* **30** 065008
- [61] Hofmans M, Viegas P, van Rooij O, Klarenaar B, Guaitella O, Bourdon A and Sobota A 2020 Characterization of a kHz atmospheric pressure plasma jet: comparison of discharge propagation parameters in experiments and simulations without target *Plasma Sources Sci. Technol.* **29** 034003

- [62] Lietz A M and Kushner M J 2018 Electrode configurations in atmospheric pressure plasma jets: production of reactive species *Plasma Sources Sci. Technol.* **27** 105020
- [63] Luo Y, Lietz A M, Yatom S, Kushner M J and Bruggeman P J 2018 Plasma kinetics in a nanosecond pulsed filamentary discharge sustained in Ar–H<sub>2</sub>O and H<sub>2</sub>O J. *Phys. D: Appl. Phys.* **52** 044003
- [64] Grubert G K, Becker M M and Loffhagen D 2009 Why the local-mean-energy approximation should be used in hydrodynamic plasma descriptions instead of the local-field approximation *Phys. Rev. E* **80** 036405
- [65] Park S-K and Economou D J 1990 Analysis of low pressure rf glow discharges using a continuum model *J. Appl. Phys.* **68** 3904–15
- [66] Capitelli M, Colonna G, D'Ammando G, Hassouni K, Laricchiuta A and Daniela Pietanza L 2017 Coupling of plasma chemistry, vibrational kinetics, collisional-radiative models and electron energy distribution function under non-equilibrium conditions *Plasma Process. Polym.* **14** 1600109
- [67] Lieberman M A and Lichtenberg A J 2005 *Principles of Plasma Discharges and Materials Processing* (Wiley)
- [68] Chantry P J 1987 A simple formula for diffusion calculations involving wall reflection and low density *J. Appl. Phys.* **62** 1141
- [69] Kemaneci E, Carbone E, Booth J-P, Graef W, van Dijk J and Kroesen G 2014 Global (volume-averaged) model of inductively coupled chlorine plasma: Influence of Cl wall recombination and external heating on continuous and pulse-modulated plasmas *Plasma Sources Sci. Technol.* **23** 045002
- [70] Thorsteinsson E G and Tomas Gudmundsson J 2009 A global (volume averaged) model of a nitrogen discharge: I. Steady state *Plasma Sources Sci. Technol.* **18** 045001
- [71] Kemaneci E H 2014 Modelling of plasmas with complex chemistry: application to microwave deposition reactors *PhD Thesis* TUE
- [72] IST-Lisbon database 2023 (available at: [www.lxcat.net](http://www.lxcat.net)) (Accesses 30 January 2023)
- [73] Levaton J, Klein A N and Amorim J 2020 Kinetic investigation of N<sub>2</sub> flowing DC discharges *Phys. Plasmas* **27** 063503
- [74] Black G, Wise H, Schechter S and Sharpless R L 1974 Measurements of vibrationally excited molecules by Raman scattering. II. Surface deactivation of vibrationally excited N<sub>2</sub> *J. Chem. Phys.* **60** 3526–36
- [75] Laporta V, Little D A, Celiberto R and Tennyson J 2014 Electron-impact resonant vibrational excitation and dissociation processes involving vibrationally excited N<sub>2</sub> molecules *Plasma Sources Sci. Technol.* **23** 065002
- [76] Database of the European union phys4entry project (available at: <http://users.ba.cnr.it/imip/cscpal38/phys4entry/database.html>) (Accessed 2020)
- [77] Guerra V, del Caz A T, Pintassilgo C D and Alves L L 2019 Modelling N<sub>2</sub>-O<sub>2</sub> plasmas: volume and surface kinetics *Plasma Sources Sci. Technol.* **28** 073001
- [78] Schwartz R N, Slawsky Z I and Herzfeld K F 1952 Calculation of vibrational relaxation times in gases *J. Chem. Phys.* **20** 1591–9
- [79] Bray K N C 1968 Vibrational relaxation of anharmonic oscillator molecules: Relaxation under isothermal conditions *J. Phys. B: At. Mol. Phys.* **1** 705–17
- [80] Alves L L, Marques L, Pintassilgo C D, Wattiaux G, Et Es-sebbar J B, Kovacević E, Carrasco N, Boufendi L and Cernogora G 2012 Capacitively coupled radio-frequency discharges in nitrogen at low pressures *Plasma Sources Sci. Technol.* **21** 045008
- [81] Laher R R and Gilmore F R 1991 Improved fits for the vibrational and rotational constants of many states of nitrogen and oxygen *J. Phys. Chem. Ref. Data* **20** 685–712
- [82] Keck J and Carrier G 1965 Diffusion theory of nonequilibrium dissociation and recombination *J. Chem. Phys.* **43** 2284–98
- [83] Capitelli M, Ferreira C M, Gordiets B F and Osipov A I 2001 Book review: Plasma kinetics in atmospheric gases *Plasma Phys. Control. Fusion* **43** 371–2
- [84] Loureiro J and Ferreira C M 1986 Coupled electron energy and vibrational distribution functions in stationary N<sub>2</sub> discharges *J. Phys. D: Appl. Phys.* **19** 17
- [85] Adamovich I V, Macheret S O, William Rich J and Treanor C E 1998 Vibrational energy transfer rates using a forced harmonic oscillator model *J. Thermophys. Heat Transfer* **12** 57–65
- [86] Adamovich I V 2001 Three-dimensional analytic model of vibrational energy transfer in molecule-molecule collisions *AIAA J.* **39** 1916–25
- [87] Ahn T, Adamovich I V and Lempert W R 2004 Determination of nitrogen V-V transfer rates by stimulated raman pumping *Chem. Phys.* **298** 233–40
- [88] National Institute of Standards and Technology 2020 Computational chemistry comparison and benchmark database (available at: <https://cccbdb.nist.gov/exp2x.asp?casno=7727379>) Standard Reference Database 101
- [89] Billing G D and Fisher E R 1979 VV and VT rate coefficients in N<sub>2</sub> by a quantum-classical model *Chem. Phys.* **43** 395–401
- [90] Capitelli M 1986 *Nonequilibrium Vibrational Kinetics* (Springer)
- [91] Capitelli M, Gorse C and Billing G D 1980 V-v pumping up in non-equilibrium nitrogen: Effects on the dissociation rate *Chem. Phys.* **52** 299–304
- [92] Esposito F, Armenise I and Capitelli M 2006 N-N<sub>2</sub> state to state vibrational-relaxation and dissociation rates based on quasiclassical calculations *Chem. Phys.* **331** 1–8
- [93] Thorsteinsson E G 2008 The nitrogen discharge: a global (volume averaged) model study *MSc Thesis* University of Iceland
- [94] Tian C and Vidal C R 1998 Electron impact ionization of N<sub>2</sub> and O<sub>2</sub>: contributions from different dissociation channels of multiply ionized molecules *J. Phys. B: At. Mol. Opt. Phys.* **31** 5369
- [95] Kossyi I A, Yu Kostinsky A, Matveyev A A and Silakov V P 1992 Kinetic scheme of the non-equilibrium discharge in nitrogen-oxygen mixtures *Plasma Sources Sci. Technol.* **1** 207
- [96] Jun Kim H, Yang W and Joo J 2015 Effect of electrode spacing on the density distributions of electrons, ions and metastable and radical molecules in SiH<sub>4</sub>/NH<sub>3</sub>/N<sub>2</sub>/He capacitively coupled plasmas *J. Appl. Phys.* **118** 043304
- [97] Bogaerts A 2009 Hybrid monte carlo—fluid model for studying the effects of nitrogen addition to argon glow discharges *Spectrochim. Acta B* **64** 126–40
- [98] Van Gaens W and Bogaerts A 2013 Kinetic modelling for an atmospheric pressure argon plasma jet in humid air *J. Phys. D: Appl. Phys.* **46** 275201
- [99] Lazarou C, Anastassiou C, Topala I, Chiper A S, Mihaila I, Pohoata V and Georghiou G E 2018 Numerical simulation of capillary helium and helium-oxygen atmospheric pressure plasma jets: propagation dynamics and interaction with dielectric *Plasma Sources Sci. Technol.* **27** 105007
- [100] Gordiets B, Ferreira C M, Pinheiro M J and Ricard A 1998 Self-consistent kinetic model of low-pressure - flowing discharges: I. volume processes *Plasma Sources Sci. Technol.* **7** 363

- [101] Henriques J, Tatarova E, Guerra V and Ferreira C M 2002 Wave driven  $N_2$ -Ar discharge. I. Self-consistent theoretical model *J. Appl. Phys.* **91** 5622–31
- [102] Piper L G 1989 The excitation of  $N(^2P)$  by  $N_2(A^3\Sigma_u^+, v' = 0, 1)$  *J. Chem. Phys.* **90** 7087–95
- [103] Clark W G and Setser D W 1980 Energy transfer reactions of  $N_2(A^3\Sigma_u^+)$ . 5. Quenching by hydrogen halides, methyl halides and other molecules *J. Phys. Chem.* **84** 2225–33
- [104] Levron D and Phelps A V 1978 Quenching of  $N_2(A^3\Sigma_u^+, v = 0, 1)$  by  $N_2$ , Ar and  $H_2$  *J. Chem. Phys.* **69** 2260–2
- [105] Guerra V and Loureiro J 1997 Electron and heavy particle kinetics in a low-pressure nitrogen glow discharge *Plasma Sources Sci. Technol.* **6** 361
- [106] Piper L G 1992 Energy transfer studies on  $N_2(X^1\Sigma_g^+, v)$  and  $N_2(B^3\Pi_g, v)$  *J. Chem. Phys.* **97** 270–5
- [107] Dreyer J W and Perner D 1972 The deactivation of  $N_2B^3\Pi_g, v = 0-2$  and  $N_2a^1\Sigma_u^-, v = 0$  by nitrogen *Chem. Phys. Lett.* **16** 169–73
- [108] Piper L G 1988 State-to-state  $N_2(A^3\Sigma_u^+)$  energy pooling reactions. II. The formation and quenching of  $N_2(B^3\Pi_g, v' = 1-12)$  *J. Chem. Phys.* **88** 6911–21
- [109] Piper L G 1989 The excitation of  $N_2(B^3\Pi_g, v = 1-12)$  in the reaction between  $N_2(A^3\Sigma_u^+)$  and  $N_2(X, v \geq 5)$  *J. Chem. Phys.* **91** 864–73
- [110] Pancheshnyi S V, Starikovskaia S M, Yu A S 1998 Measurements of rate constants of the  $N_2(C^3\Pi_u, v' = 0)$  and  $N_2^+(B^2\Sigma_u^+, v' = 0)$  deactivation by  $N_2$ ,  $O_2$ ,  $H_2$ , CO and  $H_2O$  molecules in afterglow of the nanosecond discharge *Chem. Phys. Lett.* **294** 523–7
- [111] Matveyev A A and Silakov V P 1999 Theoretical study of the role of ultraviolet radiation of the non-equilibrium plasma in the dynamics of the microwave discharge in molecular nitrogen *Plasma Sources Sci. Technol.* **8** 162
- [112] Gordiets B F, Ferreira C M, Guerra V L, Loureiro J M A H, Nahorny J, Pagnon D, Touzeau M and Vialle M 1995 Kinetic model of a low-pressure  $N_2$ - $O_2$  flowing glow discharge *IEEE Trans. Plasma Sci.* **23** 750–68
- [113] Salmon A, Popov N A, Stancu G D and Laux C O 2018 Quenching rate of  $N(^2P)$  atoms in a nitrogen afterglow at atmospheric pressure *J. Phys. D: Appl. Phys.* **51** 314001
- [114] Volynets A V, Lopaev D V, Rakhimova T V, Chukalovsky A A, Mankelevich Y A, Popov N A, Zotovich A I and Rakhimov A T 2018  $N_2$  dissociation and kinetics of  $N(^4S)$  atoms in nitrogen DC glow discharge *J. Phys. D: Appl. Phys.* **51** 364002
- [115] Piper L G 1988 State-to-state  $N_2(A^3\Sigma_u^+)$  energy-pooling reactions. I. The formation of  $N_2(C^3\Pi_u)$  and the Herman infrared system *J. Chem. Phys.* **88** 231–9
- [116] Heidner R F, Sutton D G and Suchard S N 1976 Kinetic study of  $N_2(B^3\Pi_g, v)$  quenching by laser-induced fluorescence *Chem. Phys. Lett.* **37** 243–8
- [117] Nagpal R and Ghosh P K 1990 Electron energy distribution functions and vibrational population densities of excited electronic states in DC discharges through nitrogen *J. Phys. D: Appl. Phys.* **23** 1663
- [118] Morrill J S and Benesch W M 1994 Role of  $N_2(A'^5\Sigma_g^+)$  in the enhancement of  $N_2B^3\Pi_g(V = 10)$  populations in the afterglow *J. Chem. Phys.* **101** 6529–37
- [119] Piper L G 1987 Quenching rate coefficients for  $N_2(a'^1\Sigma_u^-)$  *J. Chem. Phys.* **87** 1625–9
- [120] Freund R S 1972 Radiative Lifetime of  $N_2(a^1\Pi_g)$  and the Formation of Metastable  $N_2(a'^1\Sigma_u^-)$  *J. Chem. Phys.* **56** 4344–51
- [121] Marinelli W J, Kessler W J, David Green B and Blumberg W A M 1989 Quenching of  $N_2(a^1\Pi_g, v' = 0)$  by  $N_2$ ,  $O_2$ , CO,  $CO_2$ ,  $CH_4$ ,  $H_2$  and Ar *J. Chem. Phys.* **90** 2167–73
- [122] Lofthus A and Paul H K 1977 The spectrum of molecular nitrogen *J. Phys. Chem. Ref. Data* **6** 113–307
- [123] Wedding A B, Borysow J and Phelps A V 1993  $N_2(a'^1\Sigma_g^+)$  metastable collisional destruction and rotational excitation transfer by  $N_2$  *J. Chem. Phys.* **98** 6227–34
- [124] Tálský A, Štec O, Pazderka M and Kudrle V 2017 Kinetic study of atmospheric pressure nitrogen plasma afterglow using quantitative electron spin resonance spectroscopy *J. Spectroscopy* **2017** 5473874